PANCHROMATIC ESTIMATION OF STAR FORMATION RATES IN BzK GALAXIES AT 1 < z < 3

Citation: Kurczynski, Peter, Eric Gawiser, Minh Huynh, Rob J. Ivison, Ezequiel Treister, Ian Smail, Guillermo A. Blanc, et al. "PANCHROMATIC ESTIMATION OF STAR FORMATION RATES IN BzK GALAXIES AT 1 < z < 3." The Astrophysical Journal 750, no. 2 (April 23, 2012): 117. © 2012 The American Astronomical Society

As Published: http://dx.doi.org/10.1088/0004-637x/750/2/117

Publisher: IOP Publishing

Persistent URL: http://hdl.handle.net/1721.1/95501

Version: Final published version: final published article, as it appeared in a journal, conference proceedings, or other formally published context

The Astrophysical Journal, 750:117 (15pp), 2012 May 10 doi:10.1088/0004-637X/750/2/117

PANCHROMATIC ESTIMATION OF STAR FORMATION RATES IN *BzK* GALAXIES AT $1 < z < 3$

Peter Kurczynski[1], Eric Gawiser[1], Minh Huynh[2,3], Rob J. Ivison[4], Ezequiel Treister[5,6], Ian Smail[7], Guillermo A. Blanc[8], Carolin N. Cardamone[9], Thomas R. Greve[10], Eva Schinnerer[10], Meg Urry[11], and Paul van der Werf[10,12]

[1] Department of Physics and Astronomy, Rutgers University, Piscataway, NJ 08854, USA
[2] International Centre for Radio Astronomy Research, University of Western Australia M468, 35 Stirling Highway, Crawley, WA 6009, Australia
[3] Infrared Processing and Analysis Center, MS 220-6, California Institute of Technology, Pasadena, CA 91125, USA
[4] UK Astronomy Technology Centre, Royal Observatory, Blackford Hill, Edinburgh EH9 3HJ, UK
[5] Institute for Astronomy, University of Hawaii, 2680 Woodlawn Drive, Honolulu, HI 96822, USA
[6] Departamento de Astronomía, Universidad de Concepción, Casilla 160-C, Concepción, Chile
[7] Institute for Computational Cosmology, Department of Physics, Durham University, South Road, Durham DH1 3LE, UK
[8] Department of Astronomy, The University of Texas at Austin, Austin, TX, USA
[9] Physics Department, Massachusetts Institute of Technology, Cambridge, MA 02139, USA
[10] MPI for Astronomy, Königstuhl 17, 69117 Heidelberg, Germany
[11] Department of Physics, Yale University, P.O. Box 208121, New Haven, CT 06520-8121, USA
[12] Leiden Observatory, Leiden University, P.O. Box 9513, NL-2300 RA Leiden, The Netherlands
Received 2011 December 13; accepted 2012 February 29; published 2012 April 23

ABSTRACT

We determine star formation rates (SFRs) in a sample of color-selected, star-forming (s*BzK*) galaxies ($K_{AB} < 21.8$) in the Extended Chandra Deep Field-South. To identify and avoid active galactic nuclei, we use X-ray, IRAC color, and IR/radio flux ratio selection methods. Photometric redshift-binned, average flux densities are measured with stacking analyses in *Spitzer*-MIPS IR, BLAST and APEX/LABOCA submillimeter, VLA and GMRT radio, and *Chandra* X-ray data. We include averages of aperture fluxes in MUSYC *UBVRIz′JHK* images to determine UV-through-radio spectral energy distributions. We determine the total IR luminosities and compare SFR calibrations from FIR, 24 μm, UV, radio, and X-ray wavebands. We find consistency with our best estimator, SFR_{IR+UV}, to within errors for the preferred radio SFR calibration. Our results imply that 24 μm only and X-ray SFR estimates should be applied to high-redshift galaxies with caution. Average IR luminosities are consistent with luminous infrared galaxies. We find SFR_{IR+UV} for our stacked s*BzK*s at median redshifts 1.4, 1.8, and 2.2 to be 55 ± 6 (random error), 74 ± 8, and $154 \pm 17\ M_\odot\ \mathrm{yr}^{-1}$, respectively, with additional systematic uncertainty of a factor of $\sim$2.

Key words: galaxies: high-redshift – galaxies: statistics – infrared: general – radio continuum: general – submillimeter: general

Online-only material: color figures

1. INTRODUCTION

The history of star formation traces the origins of visible matter in the universe. Understanding star formation across cosmic time will yield insights into diverse areas of astronomy from the formation and evolution of galaxies to the initial conditions of stellar evolution. The redshift range $1 < z < 3$ is a key epoch in this history, when most of the stars in the universe were born. Galaxies in this range are identified with color selection methods. Estimating their star formation rates (SFRs) is complicated by contamination from active galactic nuclei (AGNs) and differences in luminosity to SFR calibration in the various wavebands used.[13]

SFRs are estimated from a wide variety of luminosity calibrations from X-ray through radio wavebands. Broadband UV continuum radiation directly probes the light of young stars, but is strongly attenuated by dust. The thermal IR luminosity, hereafter defined as L_{IR}, $L_{IR} \equiv L(8\text{–}1000\,\mu\mathrm{m})$, measures the SFR from the reprocessed dust emission (e.g., Kennicutt 1998b). IR and uncorrected UV luminosities represent reprocessed and unreprocessed photons and are used to estimate the total SFR.

UV slope based corrections for dust attenuation (e.g., Meurer et al. 1999) have been previously applied to high-redshift, star-forming (SF) galaxies (e.g., Reddy & Steidel 2004; Reddy et al. 2005, 2006, 2010; Daddi et al. 2007b; Magdis et al. 2010). Low-redshift analogs of Lyman break galaxies (LBGs) have similar dust attenuation corrections (Overzier et al. 2011), although ULIRGs have higher dust correction factors (Howell et al. 2010) and other SF galaxies have lower dust corrections than expected (e.g., Buat et al. 2010), and significant scatter is observed.

Radio-wave (1.4 GHz) luminosity in SF galaxies, primarily synchrotron emission from supernova remnants, also traces SFR (Condon 1992). Radio-wave SFR calibrations rely explicitly upon the IR–radio correlation (e.g., Bell 2003; Yun et al. 2001) or use an implicit conversion to Hα luminosity to calibrate SFR (Condon 1992).

X-ray emission in SF galaxies arises from low-mass X-ray binaries (LMXBs), consisting of long-lived, low-mass ($M < 1\,M_\odot$) stars with neutron star companions, high-mass X-ray binaries (HMXBs), consisting of short-lived, massive ($M > 8\,M_\odot$) stars with a neutron star companion, and to a lesser extent, supernova remnants (Persic & Rephaeli 2002). These last two sources of X-ray emission are linked to short-lived, massive stars, providing a rationale for X-ray SFR calibrations. However, these multiple sources of X-ray emission, as well as X-ray obscuration by gas and dust, complicate X-ray luminosity to SFR calibrations. In practice, X-ray SFR calibrations (e.g., Ranalli et al. 2003; Persic et al. 2004; Lehmer et al. 2010) explicitly rely upon empirical correlations with IR luminosity

[13] Other sources of systematic uncertainty include the initial mass function (IMF), photometric redshifts, and spectral energy distributions (SEDs).

and are therefore indirect measures of IR luminosity. X-ray emission from AGNs are major sources of contamination.

Daddi et al. (2007b) find SFR from dust-corrected UV, 24 μm, 1.4 GHz, and X-ray calibrations to be approximately consistent for SF (BzK; see below) galaxies at $z \sim 2$. Reddy et al. (2006) compare dust-corrected UV, 24 μm, and X-ray calibrations for a spectroscopic sample of $z \sim 2$ galaxies, and find dust-corrected UV SFR to be consistent with 24 μm SFR for BzKs, but not other types of SF galaxies.

Wuyts et al. (2011) compare dust-corrected UV, 24 μm, and *Herschel* PACS derived SED based SFRs to Hα based SFRs and find Hα derived SFRs to require extra dust correction to agree with $\mathrm{SFR_{UV+IR}}$. In addition, other recent literature has illustrated that 24 μm SFRs are overestimated for high-luminosity sources at $z \sim 2$ (Elbaz et al. 2011; Nordon et al. 2012).

Pannella et al. (2009) find radio SFR based on the calibration of Yun et al. (2001) to be consistent with dust-corrected UV SFR for BzKs.

X-ray SFRs based on the calibration of Ranalli et al. (2003) are found to agree with dust-corrected UV SFRs for BX and BM galaxies in the range $1.5 < z \leqslant 3.0$ (Reddy & Steidel 2004) and with 24 μm SFR (Reddy et al. 2006).

We seek to expand upon previous studies by including a wider range of luminosity estimates, including the most recent results from X-ray observations and analyses, and by understanding the assumptions and sources of uncertainty inherent to each SFR calibration. We seek to ascertain the extent to which submillimeter data can improve IR-based SFR estimates. We compare different radio luminosity to SFR calibrations, and we use the most recent X-ray data and luminosity to SFR calibrations. By comparing these estimates to the total SFR, derived from the sum of IR and uncorrected UV luminosity, we seek to test their robustness at high redshift.

We investigate SFRs binned according to photometric redshift, with stacking analyses in radio through X-ray wavebands. In particular, we use extensive FIR–submillimeter data for which we have an improved stacking algorithm (Kurczynski & Gawiser 2010). We discuss observations and data in Section 2. We present our stacking methodology in Section 3. Results are presented in Section 4, and we discuss comparisons of SFR in Section 5. Our conclusions are summarized in Section 6. Throughout this paper, magnitudes are measured in the AB system unless stated otherwise. We assume a Salpeter (1955) IMF from 0.1 to 100 $M_\odot$. Another commonly used IMF, that of Kroupa (2001), would change the slope of the low-mass end of the IMF and multiply the SFRs presented here by factors of 0.58 (e.g., Hopkins 2007). We adopt a cosmology with $\Omega_\Lambda = 0.7$, $\Omega_0 = 0.3$, and $h_{100} = 0.7$.

2. SAMPLE SELECTION

The BzK color selection criterion has emerged as a successful color-based method for identifying galaxies in the range $1.4 \lesssim z \lesssim 2.5$ in a maximally inclusive manner (Daddi et al. 2004). The quantity BzK[14] is defined as

$$BzK \equiv (z - K)_{\mathrm{AB}} - (B - z)_{\mathrm{AB}}. \quad (1)$$

[14] In this paper, we have corrected colors to account for differences between the Bessel B band filter used on the Very Large Telescope (VLT) in the original sample of Daddi et al. (2004) and the Johnson B band filter on WFI, Suprime-Cam, and other instruments. Not accounting for this correction can lead to an offset of 0.5 mag toward lower values in $(B - z)$ color and 0.04 mag in higher $(z - K)$ color, producing a significant excess of "sBzK" galaxies that are in fact low-redshift contaminants (Blanc et al. 2008).

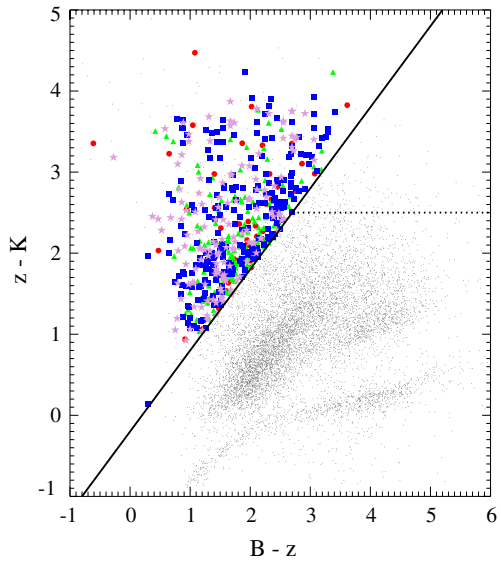

Figure 1. BzK diagram illustrating corrected NIR–optical colors $(z - K)_{\mathrm{AB}}$ vs. $(B - z)_{\mathrm{AB}}$ for MUSYC $K < 21.8$ selected sources (gray points), including redshift-binned, star-forming galaxies (with X-ray-detected AGNs removed, see the text) in the range $0.9 < z \leqslant 1.2$ (red circles), $1.2 < z \leqslant 1.5$ (green triangles), $1.5 < z \leqslant 2.0$ (blue squares), and $2.0 < z \leqslant 3.2$ (purple stars). The sBzK region is located above the diagonal line and is defined as $BzK \geqslant 0.2$. The $pBzK$ region is the wedge-shaped area above the horizontal dotted line, $z - K > 2.5$.

(A color version of this figure is available in the online journal.)

Actively SF galaxies, sBzKs, are found to satisfy $BzK > -0.2$, the upper left region in Figure 1. The reddening vector in the BzK plane is parallel to the BzK line, making this selection unbiased with respect to dust content. In this paper, we ignore the reddest galaxies in both $z - K$ and $B - z$, pBzKs, which tend to be old, passively evolving stellar systems, and are located in the upper right region of Figure 1. Comparisons and overlaps between BzKs and other color-selected galaxy types are discussed in Reddy et al. (2005), Grazian et al. (2007), and Greve et al. (2010). SFR estimates typically range from several tens to hundreds $M_\odot$ yr^{-1} (e.g., Daddi et al. 2004, 2005, 2007b; Reddy et al. 2005, 2006; Dunne et al. 2009; Pannella et al. 2009; Greve et al. 2010; Yoshikawa et al. 2010).

Our sample of sBzK galaxies with $K_{\mathrm{Vega}} < 20$ ($K_{\mathrm{AB}} < 21.8$) comes from the catalog of Blanc et al. (2008) and is taken from the Multiwavelength Survey by Yale-Chile (MUSYC; Gawiser et al. 2006) observations of the Extended Chandra Deep Field-South (ECDF-S). Photometry in the $UBVRIz'JHK$ wavebands is obtained from the K-selected catalog of Taylor et al. (2009) and is augmented with data from the MUSYC optical catalog ($R_{\mathrm{AB}} < 25.3$ depth; Cardamone et al. 2010), which includes photometry from 32 bands including 18 medium band optical filters and *Spitzer* Infrared Array Camera (IRAC) bands.

We use X-ray luminosity, IRAC colors, and q_{IR} criteria to discriminate SF galaxies from AGNs. There are 110 BzK sources detected in the combined 250 ks (Virani et al. 2006) + 4 Ms (Xue et al. 2011) *Chandra* catalogs. Of these sources, 61 are in the Chandra Deep Field-South (CDF-S), and the remaining 49 are in the ECDF-S. X-ray luminosity is used to distinguish AGNs from SF galaxies (e.g., Nandra et al. 2002):

$$L(\mathrm{AGN;\ 2\text{–}10\,keV}) > 10^{42}\ \mathrm{erg\ s^{-1}}. \quad (2)$$

There are 107/110 X-ray detected BzKs that meet this criterion (three X-ray detected BzKs in the 4 Ms CDF-S have

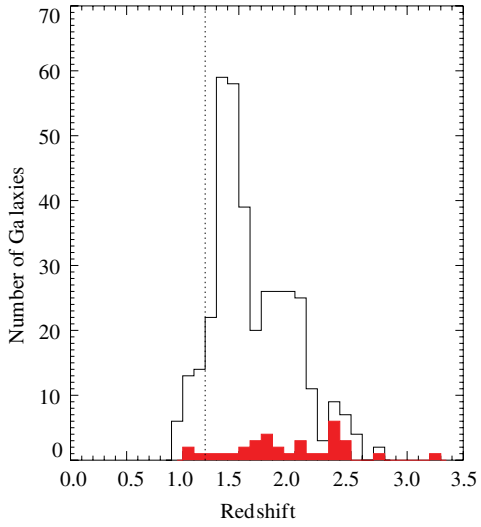

Figure 2. Histograms of photometric and spectroscopic redshifts for s*BzK* galaxies in ECDF-S. The upper histogram indicates photometric redshifts. The lower filled (red) histogram indicates spectroscopic redshifts. The vertical dotted line demarcates $z < 1.2$ galaxies that are excluded from analysis.

(A color version of this figure is available in the online journal.)

Table 1
Summary of Results of AGN Selection Criteria Applied to s*BzK* Sample

Test	Detected	AGN	X-ray	q_{IR}	IRAC
(1)	(2)	(3)	(4)	(5)	(6)
X-ray	110	107	**83**	7	18
q_{IR}	35	22	7	**15**	2
IRAC	649	25	18	2	**7**

Notes. Column 1 indicates the waveband test used for AGN discrimination. Column 2 indicates the number of sources with data in each respective waveband. Column 3 indicates the number of AGNs confirmed by each waveband test irrespective of tests in other wavebands. Entries in Columns 4–6 indicate the number of sources classified as AGNs according to each waveband as follows: diagonal entries (in boldface) indicate sources that are uniquely identified as AGNs in only one waveband. Off diagonal entries indicate sources that are identified as AGNs in at least the two wavebands indicated by the respective row and column headings.

$L_X < 10^{42}$ erg s^{-1} and are considered SF galaxies in this analysis). Twenty-five *BzK*s were identified as AGNs on the basis of their position in IRAC color–color space (Donley et al. 2012). Finally, we computed q_{IR} values, defined as the ratio of integrated IR flux, FIR (8–1000 μm; rest frame; W m^{-2}) to radio flux density, $F_{1.4\,GHz}$ (rest frame; W m^{-2} Hz^{-1}; e.g., Ivison et al. 2010b):

$$q_{IR} = \log(\mathrm{FIR}/3.75 \times 10^{12}\,\mathrm{Hz}/F_{1.4\,GHz}). \quad (3)$$

Radio-loud AGNs are discriminated from radio-quiet AGNs/SF galaxies according to Ivison et al. (2010b):

$$q_{IR}(\mathrm{AGN}) < 2.0. \quad (4)$$

Computing q_{IR} for *BzK*s requires sufficient photometry to estimate the rest-frame FIR SED. Observed frame SEDs for *BzK*s with IRAC+MIPS24+VLA detections were fit to Chary & Elbaz (2001, hereafter CE01) templates. Rest-frame radio luminosities were estimated by assuming an $S_\nu \sim \nu^\alpha, \alpha = -0.8$ radio SED, characteristic of SF galaxies (Condon 1992). Thirty-five sources were identified as AGNs using the q_{IR} criterion; 15 of these sources are uniquely identified as AGNs with this method, and the remainder are also identified as AGNs using other methods.

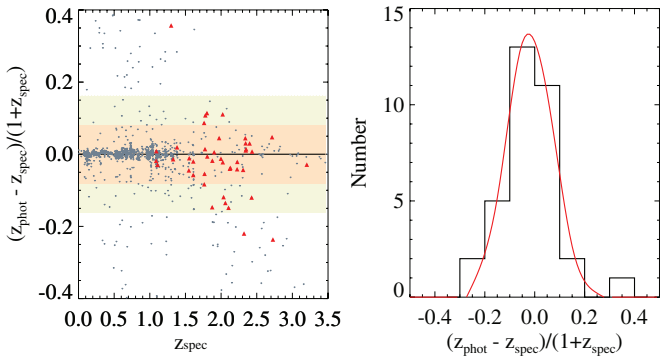

Figure 3. Left panel illustrates photometric redshift error, defined as $(z_{phot} - z_{spec})/(1 + z_{spec})$, vs. spectroscopic redshift for *K*-selected galaxies in ECDF-S. Triangles (red) illustrate s*BzK* galaxies. 1σ and 2σ regions, determined from the fit to the histogram (right panel), are indicated by shading. Points (gray) illustrate all 1285 *K* selected galaxies for which spectroscopic and photometric redshifts are available. The right panel illustrates histogram of photometric redshift errors for s*BzK* galaxies along with a Gaussian fit (mean $= -0.02$ and $\sigma = 0.09$).

(A color version of this figure is available in the online journal.)

A summary of the results of AGN rejection methods is given in Table 1. Sources identified as AGNs are excluded from the remaining analysis. At present it is not possible to conclusively identify all AGNs including deeply obscured sources; however, these methods make the best use of available data. Effects of possible residual AGN contamination are discussed in Section 5.

Photometric or spectroscopic redshifts are assigned to s*BzK* galaxies by matching positions in the *K*-band source catalog with the MUSYC optical catalog and using redshifts from the optical catalog where redshifts in both catalogs are available. Photometric redshifts for the optical catalog were obtained with the EAzY software (Brammer et al. 2008); the reader is referred to Cardamone et al. (2010) for details of the redshift determination.

Histograms of photometric and spectroscopic redshifts are illustrated in Figure 2. These histograms indicate that the majority of s*BzK*s fall in the traditional redshift range associated with *BzK* galaxies, $1.4 < z < 2.5$. There are significant numbers of s*BzK*s at lower (20%) and higher (4%) redshifts, although *BzK* selection is less efficient in these ranges. Spectroscopic redshifts are taken from the literature for which there are substantial selection biases; therefore, we do not expect the distribution of spectroscopic redshifts to match precisely the distribution of photometric redshifts. Thus, the trend of spectroscopic redshifts being distributed at somewhat higher redshifts than the photometric redshifts, apparent from Figure 2, is not an indication of systematic photometric redshift error.

There are 48 galaxies in the range $1.2 < z < 3.3$ that have spectroscopic and photometric redshifts available. Photometric redshift errors, defined as $(z_{phot} - z_{spec})/(1 + z_{spec})$, are well described by a Gaussian with mean $= -0.02$ and $\sigma = 0.09$; see Figure 3. Photometric redshift errors for these galaxies are plotted versus spectroscopic redshift in Figure 3 and compared to the distribution of photometric redshift errors for the larger sample of 1285 *K*-selected galaxies with both redshifts available. The 1σ and 2σ regions are indicated by shading in the figure. Three s*BzK* galaxies have photometric redshifts that are more than 2σ outliers; this outlier fraction is consistent with Gaussian statistics given our sample size.

Table 2
Redshift Binned Sample of Non-AGN Star-forming Galaxies (s*BzK*s) in the ECDF-S

	Total Sample		Individual Detections				
Redshift Range (1)	Median Redshift (2)	Number (z_{phot}, z_{spec}) (3)	MIPS (24 μm) (4)	MIPS (70 μm) (5)	LESS (870 μm) (6)	VLA (1.4 GHz) (7)	*Chandra* (0.5–2 keV) (8)
$1.2 < z \leqslant 1.5$	1.383	156 (152,4)	64	4	2	2	1
$1.5 < z \leqslant 2.0$	1.753	215 (202,13)	90	9	6	9	1
$2.0 < z \leqslant 3.2$	2.272	139 (122,17)	61	1	1	5	0

Notes. Redshift binning scheme selected for this analysis. Column 1 indicates the redshift range for each bin. Column 2 indicates the median redshift of the sampled galaxies in each bin. Column 3 shows the total number of galaxies in each bin, with numbers of photometric and spectroscopic redshifts, respectively, in parentheses. Columns 4–8 indicate the number of sources that are individually detected in each waveband; fluxes from individual detections are combined with stacked fluxes of the remaining sources in each redshift bin, as discussed in the text and the Appendix.

The final sample of 510 star-forming s*BzK*s with redshift $1.2 < z \leqslant 3.2$ are binned according to redshift into approximately 1 Gyr intervals in cosmic time: $1.2 < z \leqslant 1.5$, $1.5 < z \leqslant 2.0$, and $2.0 < z \leqslant 3.2$; details are included in Table 2. These sets of galaxies are used in analysis of individual detections and combined non-detections (stacking analyses) to determine their aggregate fluxes in each waveband.

The redshift-binned sets are illustrated in a *BzK* diagram in Figure 1. $(B - z)$ and $(z - K)$ colors for these galaxies are determined from flux values given in the catalog of Blanc et al. (2008). Non-detections in the B band lead to undetermined $(B - z)$ colors for 4 and 13 galaxies in the redshift bins $1.5 < z \leqslant 2.0$ and $2.0 < z \leqslant 3.2$, respectively. These galaxies are excluded from Figure 1.

3. MULTIWAVELENGTH ANALYSES AND STACKING ANALYSES

We measure the redshift-bin-averaged multiwavelength SEDs of our sample and use these data to estimate SFRs using published broadband calibrations. Most of these galaxies are not individually detected in far IR–radio and X-ray wavebands; therefore stacking analysis, using the K-band positional priors, is essential. The same analysis method is used for stacking in each IR–radio waveband: an ordinary average of fluxes of individual detections and the stacking detection yields an aggregate flux estimate for each redshift bin. As discussed in the Appendix, a weighted average of individual and stacking detections may introduce a bias toward dim sources. The same set of galaxies are analyzed in all wavebands with the exception of X-ray in which only sources in the CDF-S are studied. We do not expect the additional position selection criterion of these sources to introduce any bias. Furthermore, as discussed in Section 3.4, galaxies in the CDF-S will dominate the stacking signal of sources in the full ECDF-S due to the greater X-ray exposure in CDF-S.

3.1. IR–Submillimeter

MIPS 24, 70 μm. Infrared data were obtained from the *Spitzer Space Telescope* Multi Band Imaging Photometer (MIPS) 24 μm and 70 μm images that reach 5σ depths of 50 μJy and 3 mJy, respectively (Magnelli et al. 2009). The K-band s*BzK* positions are compared to the 24 μm (70 μm) catalog, with positions less than $2''$ ($4''$) separation as the criterion for matching to individual detection in each MIPS band, respectively. Individual detections are removed from the list for stacking and incorporated into the analysis subsequently. In 24 μm data, in redshift bins from $1.2 < z \leqslant 1.5$, $1.5 < z \leqslant 2.0$, and $2.0 < z \leqslant 3.2$, there are 64, 90, and 61 individual detections and 92, 125, and 78 stacked positions, respectively. Similarly, in 70 μm data, in these same redshift bins, there are 4, 9, and 1 individual detections and 151, 205, and 136 stacked positions in each of the redshift bins (1, 1, and 2 sources, respectively, could not be analyzed due to their being on the edge of the 70 μm image). Stacking is performed on a residual image, after removing the matched sources from the list, as summarized in Huynh et al. (2007). The stacking algorithm computes an inverse variance weighted average of the flux at each stack position. We use an ordinary average of the individual detections and the stacking detection to yield a single combined estimate for the flux of each set of galaxies. We show in the Appendix that, although the difference between these two approaches is small, the ordinary average is preferred because the weighted average can introduce a bias to the combined flux estimate.

BLAST 250, 350, 500 μm. Submillimeter data at 250, 350, and 500 μm were obtained from the public archive of the Balloon-borne Large Area Space Telescope (BLAST) survey of the ECDF-S, which reaches 1σ depths of 36, 31, and 20 mJy at 250, 350, and 500 μm, respectively, in an 8.7 deg^2 wide field and 1σ depths of 11, 9, and 6 mJy at 250, 350, and 500 μm in a 0.8 deg^2 deep field (Devlin et al. 2009).

The redshift-binned s*BzK*s are stacked in the public BLAST "smooth" data (variance-weighted correlation between the signal maps and the effective point-spread functions, PSFs). Each pixel in these data products represents the maximum likelihood flux density (Jy) of an isolated point source centered over the pixel (Truch et al. 2008).

We use an improved submillimeter stacking and deblending algorithm for stacking in 250, 350, 500, and 870 μm data that deal effectively with the problem of confusion (Kurczynski & Gawiser 2010). Confusion severely limits the effectiveness of stacking in deep surveys with limited angular resolution (Condon 1974; Hogg 2001), particularly at far IR–submillimeter wavelengths, and causes a bias in stacking results. Deblending corrects measured fluxes for confusion from these adjacent sources. This stacking and deblending algorithm greatly reduces bias in the flux estimate with nearly minimum variance. For more details, see Kurczynski & Gawiser (2010). All galaxies in the MUSYC catalog with $K_{AB} < 22$ are used in the deblending calculations.

We find stacking detections (defined as S/N $\geqslant$ 3) in the 250 μm data for the redshift bin $1.5 < z \leqslant 2.0$ (stacking detection S/N = 12), and in the 350 μm data for the redshift bins $1.2 < z \leqslant 1.5$ (S/N = 3) and $1.5 < z \leqslant 2.0$ (S/N = 10), and in the 500 μm data, for the redshift bin $1.5 < z \leqslant 2.0$ (S/N = 10). See Table 3 for the stacked flux densities and errors in each

Table 3
UV–Radio Average Flux Densities for Redshift-binned s*BzK*s

		$1.2 < z \leqslant 1.5$		$1.5 < z \leqslant 2.0$		$2.0 < z \leqslant 3.2$	
Band	λ	S_ν	σ_S	S_ν	σ_S	S_ν	σ_S
(1)	(2)	(3)	(4)	(5)	(6)	(7)	(8)
U	0.35	0.45	0.06	0.36	0.05	0.27	0.05
B	0.46	0.61	0.04	0.58	0.04	0.59	0.04
V	0.54	0.65	0.04	0.67	0.04	0.73	0.05
R	0.65	0.85	0.05	0.80	0.05	0.86	0.05
I	0.86	1.57	0.17	1.36	0.16	1.16	0.16
z	0.90	1.63	0.24	1.34	0.23	1.18	0.24
J	1.25	3.77	0.63	4.31	0.63	2.79	0.61
H	1.65	4.25	0.79	4.97	0.80	3.52	0.71
K	2.13	9.70	1.24	10.32	1.22	9.69	1.24
24 μm	24	94	2	110	2.0	120	2.1
70 μm	70	320	81	340	83	440	85
250 μm	250	2000	880	9080	750	1400	930
350 μm	350	2020	690	5700	590	920	730
500 μm	500	1030	480	4300	400	1300	510
870 μm	870	240	94	510	80	530	100
1.4 GHz	214000	15	0.8	12	0.7	15	0.8
610 MHz	490000	27	5.2	32	4.3	15	5.3

Notes. Column 1: waveband; Column 2: effective, observed frame wavelength in units of μm; Columns 3, 5, 7, and 9: average, observed flux density in units of μJy for each redshift bin; Column 4, 6, 8, and 10: error in flux density in units of μJy for each redshift bin.

waveband. In the SED fits discussed below, the measured fluxes of formal non-detections and their appropriate error bars are included in the fits. Combining all of the *BzK* galaxies, without regard to redshift binning, yields stacking detections in 250, 350, and 500 μm data of 3.9 ± 0.4 mJy, 2.5 ± 0.3 mJy, and 1.8 ± 0.2 mJy, respectively.

Fluxes reported from stacking 24 μm selected *BzK* galaxies in the same field, with a different stacking algorithm, are larger by about a factor of two than those values presented here (Marsden et al. 2009); in addition to the difference in selection of the present sample (which is *K* selected and excludes AGNs), this discrepancy may also possibly be attributed to lack of deblending in these previous reported results (Chary & Pope 2010).

LESS 870 μm. Submillimeter data at 870 μm were obtained from the Large Apex Bolometer Camera ECDF-S Submillimeter Survey (LESS; Weiß et al. 2009), which reaches a 1σ depth of approximately 1.2 mJy beam^{-1}. The LESS catalog contains 126 individually detected submillimeter sources (Weiß et al. 2009) and these data have been used previously for stacking analyses of *BzK* galaxies (Greve et al. 2010).

The redshift-binned s*BzK*s are stacked in the beam-smoothed, flux map (Weiß et al. 2009); galaxies in the MUSYC *K*-band catalog are used in the deblending calculations. Individual detections, as identified through 1.4 GHz and/or MIPS 24 μm counterparts (Biggs et al. 2011), are excluded from the stacking/deblending analysis and incorporated into the aggregate (stacking + individual detections) flux estimates as discussed above and in the Appendix. There were 2, 6, and 1 individual 870 μm detections in the $1.2 < z \leqslant 1.5$, $1.5 < z \leqslant 2.0$, and $2.0 < z \leqslant 3.2$ bins, respectively. These individual detections contributed 46%, 29%, and 9% to the aggregate (individual + stacking) detection, respectively. Stacked flux estimates are <282 (3σ), 509 ± 80, and 533 ± 100 μJy in the $1.2 < z \leqslant 1.5$, $1.5 < z \leqslant 2.0$, and $2.0 < z \leqslant 3.2$ bins. These stacked flux estimates are combined with individual fluxes into the aggregate values indicated in Table 3.

Table 4
Redshift-binned s*BzK* IR–Radio Fit Summary

Redshift	Fit Type	L_{IR}	χ^2(df)	SFR_{IR}
(1)	(2)	(3)	(4)	(5)
$1.2 < z \leqslant 1.5$	CE01 ($\geqslant$24 μm)	3.0 ± 0.3	48.23(7)	51 ± 5
	CE01 (>24 μm)	1.9 ± 0.2	5.92(6)	33 ± 3
	CE01 (24 μm)	4.1 ± 0.3	3.28(0)	70 ± 9
$1.5 < z \leqslant 2.0$	CE01 ($\geqslant$24 μm)	4.0 ± 0.4	100.94(7)	68 ± 7
	CE01 (>24 μm)	5.0 ± 0.9	75.31(6)	86 ± 15
	CE01 (24 μm)	8.6 ± 0.5	0.03(0)	148 ± 45
$2.0 < z \leqslant 3.2$	CE01 ($\geqslant$24 μm)	8.3 ± 0.7	51.24(7)	143 ± 12
	CE01 (>24 μm)	6.3 ± 0.7	13.23(6)	108 ± 12
	CE01 (24 μm)	35.4 ± 2.1	1.82(0)	608 ± 91

Notes. Column 1 indicates redshift range for the sample. Column 2 specifies the type of the model fit (see the text). Column 3 indicates the computed L_{IR} from the best-fit model, in units of 10^{11} $L_\odot$. Column 4 indicates the χ^2 value for the best fit, with degrees of freedom in parentheses. Column 5 indicates the SFR, in units of $M_\odot$ yr^{-1}, computed from the fit-derived IR luminosity. Random errors correspond to 68% confidence intervals and do not include substantial systematic error, as discussed in the text.

IR luminosity estimation. In order to estimate L_{IR}, we fit observed IR–radio photometry to template libraries from Chary & Elbaz (2001). We explore several approaches; in each case, a different region of the IR–radio spectrum is chosen for template fitting. Fits are performed on each redshift-bin-averaged spectrum. The template rest-frame luminosity is converted to an observed frame flux distribution at the median redshift of the redshift bin. Then the observed frame model flux distribution is convolved with each photometric bandpass transmission function to generate predicted model photometry. The predicted photometry is combined with observed photometric fluxes and errors to generate a χ^2 statistic for each fit. Each template in the library is fit in this way, with the smallest χ^2 fit chosen as the best-fit template. For fits that include observations at multiple wavelengths, an overall normalization, A, set to its analytical best-fit value via $\partial\chi^2/\partial A = 0$, is factored into the best-fit spectrum.

We explore several additional approaches to estimating L_{IR} from the data using CE01 template fits: for each redshift bin, we fit (1) the 24 μm and longer wavelength data, (2) the long-wavelength IR and radio data excluding 24 μm, and (3) 24 μm only data. Optical/NIR data are excluded from the fits because CE01 templates are considered to be incomplete for $\lambda < 1$ μm. For the 24 μm only fits, there is no free normalization factor, and the CE01 template luminosity is used directly to estimate L_{IR}. For these single-band fits, the variation of χ^2 with template index is used as the basis for determining confidence intervals; 68% error bars are found for the L_{IR} estimate, and these errors are propagated into an SFR uncertainty. These fits are illustrated in Table 4 and Figure 4, and are discussed in Section 4.

Uncertainties in L_{IR} are determined from 68% confidence intervals determined from variations in χ^2 with normalization. We considered separately the effects of error in the redshift. We approximate the error of the median redshift by computing the error of the mean of individual redshifts. This error of the mean diminishes according $1/\sqrt{N}$, where N is the number of objects in each redshift bin. We computed L_{IR} for our samples at the $\pm 1\sigma$ values of the mean redshift and found the results to be the same as the actual L_{IR} to within the normalization error. Consequently, the error in the mean redshift does not contribute significantly to the overall L_{IR} uncertainty. Because

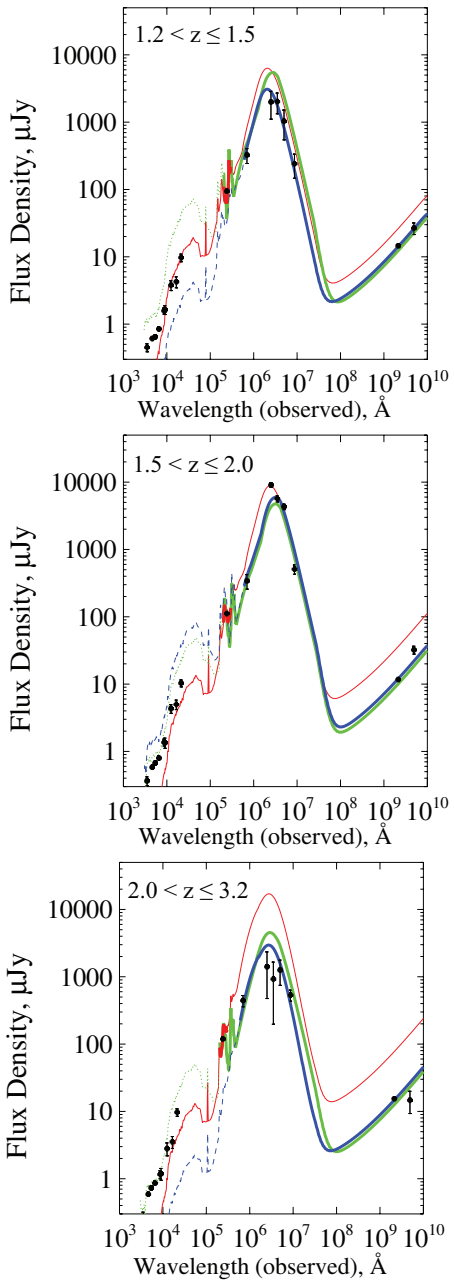

Figure 4. Spectral energy distributions of redshift-binned s*BzK* galaxies obtained from stacking analysis, and fits to various models. Spectral flux density, in units of μJy, is plotted vs. observed frame wavelength, in units of Angstroms. UV-through-radio flux measurements are indicated by points with error bars. Curves indicate best-fit models: dotted (green) CE01 template fitted to the $\lambda \geqslant 24\,\mu$m spectrum, dashed (blue) CE01 template fitted to the $\lambda > 24\,\mu$m spectrum, and solid (red) CE01 template fitted to only the $24\,\mu$m data point. For each model fit, the region of the spectrum used for the fit is indicated by the solid portion of the curve. Top: galaxies in the redshift range $1.2 < z \leqslant 1.5$; middle $1.5 < z \leqslant 2.0$; bottom $2.0 < z \leqslant 3.2$. See also Table 4 for fit details.

(A color version of this figure is available in the online journal.)

the median redshift is more robust to the presence of outliers, we consider the error of the mean to be an upper bound to the error of the median. We also address the effect of redshift and individual galaxy SED errors via simulations, as discussed in Section 3.5. On this basis, we ignore error of the median redshift in subsequent calculations.

We address the question of whether $L_{\rm IR}$ determined from the average flux SED is indicative of the true average of individual galaxy luminosities in two ways: (1) using observations of the (bright) subset of $24\,\mu$m detected sources and (2) in simulations for the entire sample including individually non-detected sources.

The redshift bin average $L_{\rm IR}$ for individually detected $24\,\mu$m sources is computed based on individual fits to CE01 templates, using only the $24\,\mu$m band photometry. Average $L_{\rm IR}$ is also computed for this $24\,\mu$m bright subset using the same procedure as used in the larger sample of *BzK*s: flux values are combined to form an unweighted average SED. This average SED is then fit to CE01 templates to determine $L_{\rm IR}$. The two $L_{\rm IR}$ estimates agree to within 10%–20% in our redshift bins. In Section 3.5, we generalize these results to our entire sample using simulations.

We use the calibration of Kennicutt (1998b) to convert $L_{\rm IR}$ to estimated SFR. This calibration is based on the starburst synthesis models of Leitherer & Heckman (1995), and it assumes a continuous burst of age 10–100 Myr, solar abundances, Salpeter IMF, and bolometric luminosity arising from dust reradiation. This calibration relates the $L_{\rm IR}$ integrated from 8–1000 μm to SFR according to

$$\mathrm{SFR_{IR}}(M_\odot\ \mathrm{yr}^{-1}) = 4.5 \times 10^{-44} L_{\rm IR}(\mathrm{erg\ s}^{-1}). \quad (5)$$

The uncertainty in this relation arises from uncertainties in the estimation of $L_{\rm IR}$ resulting from the extrapolation of observed fluxes to the total, integrated $L_{\rm IR}$, confounding sources of IR emission that are not associated with star formation, and the use of a fixed continuous burst model; the combined errors in the SFR are attributed as being a factor of ~2–3. This systematic uncertainty in luminosity to SFR conversion dominates the overall error budget in SFR estimates; the impact of this substantial systematic uncertainty on other SFR estimates, many of which depend indirectly on the $L_{\rm IR}$–SFR relationship, is discussed in Section 5. SFR estimates for our redshift-binned s*BzK*s are discussed in Section 4.1. Uncertainties in these SFR estimates include only errors in $L_{\rm IR}$ (arising from photometry and template normalization).

3.2. UV–Optical–NIR

MUSYC 5σ imaging depths include $U = 26.5$, $B = 26.9$, $V = 26.6$, $R = 26.3$, $I = 24.8$, $z' = 24.0$, $J = 23.1$, $H = 22.4$, and $K = 22.4$ as well as 18 medium band photometry in the range [4270,8560] Å (Gawiser et al. 2006; Taylor et al. 2009; Cardamone et al. 2010). Galaxies are individually measured in MUSYC *UBVRIz'JHK* bandpasses via aperture photometry, and additionally their fluxes in each redshift bin are combined in an unweighted average to yield a single averaged SED for each redshift range. These average fluxes for redshift-binned s*BzK*s in each UV–radio waveband are indicated in Table 3. IR data in the ECDF-S are available in IRAC bands at 3.6, 4.5, 5.8, and 8.0 μm (SIMPLE; Damen et al. 2011). As discussed in Section 2, IRAC data were used in photometric redshift determination; however, these data were not used in the fits to determine $L_{\rm IR}$.

To determine UV continuum luminosity before dust correction, $L_\nu^{\rm Uncorr}$, we use the available optical–NIR photometry. We estimate the rest-frame 1600 Å flux density, $f_\nu^{\rm Uncorr}$, via interpolation of the two bracketing broadband fluxes. The specific luminosity at 1500 Å , $L_\nu^{\rm Uncorr}$ in units of erg s^{-1} Hz^{-1}, at the redshift, z, is then found from the flux density, $f_\nu^{\rm Uncorr}$ in units of μJy and the luminosity distance, D_L, according to

$$L_\nu^{\rm Uncorr} = 1 \times 10^{-29} f_\nu^{\rm Uncorr} \frac{4\pi D_L^2}{(1+z)}. \quad (6)$$

To convert luminosity to SFR, we use the calibration of Kennicutt (1998a), which corresponds to the calibration of Madau et al. (1998) converted to Salpeter IMF and 0.1–100 $M_\odot$ mass limits:

$$\mathrm{SFR_{UV}}(M_\odot\,\mathrm{yr}^{-1}) = 1.4\times10^{-28}L_\nu(\mathrm{erg\,s^{-1}\,Hz^{-1}}). \quad (7)$$

This calibration assumes continuous star formation over timescales of 10^8 years or longer and solar metallicity. Kennicutt (1998a) discusses sources of systematic uncertainty in the various published L_ν–SFR calibrations as arising from the use of different stellar libraries and assumptions about the star formation timescales; the published calibrations differ by about a factor of two. We use Equation (7) to compute SFR from uncorrected luminosities, L_ν^{Uncorr}, to estimate the contribution to SFR that is unobscured by dust. We also apply this expression to dust-corrected luminosities to determine dust-corrected UV SFR, $\mathrm{SFR_{UV}^{Corr}}$, as discussed below.

To obtain dust-corrected UV SFRs, we use the method of IRX-β (Meurer et al. 1999). This method has been used in high-redshift LBGs (e.g., Meurer et al. 1999; Adelberger & Steidel 2000; Reddy et al. 2010), *BzK* galaxies (Daddi et al. 2007b), and galaxies at lower redshift (e.g., Buat et al. 2010; Howell et al. 2010; Takeuchi et al. 2010).

We fit the rest-frame UV f_λ spectrum to a power law, $f_\lambda(\lambda) = A\lambda^\beta$, using a range of trial β values: $-2.5 < \beta < 1.0$ in steps $\Delta\beta = 0.01$. Due to the availability of 18 medium band photometry, these fits typically had 12–14 sampled points in the spectrum. The wavelength range of the fits, [1268, 2580] Å in the rest frame, is chosen to be the same as that used in Calzetti et al. (1994), which Meurer et al. (1999) also adopted. These values are redshifted into the observed frame, and photometry data falling within this range are used for the fits. For each trial value of β, predicted flux values are computed at each relevant, observed wavelength by integrating over the filter bandpass transmission function, $T(\lambda)$, and intergalactic medium transmission function, $M(\lambda)$, from Madau (1995). The integral is expressed in terms of the number of photons detected, hence an extra factor of λ is included in the integrand, as illustrated below in Equation (8). The integral is normalized to units of μJy by dividing by the corresponding integral of a reference spectrum that is flat in f_ν ($f_\nu^{\mathrm{ref}} = 1\,\mu$Jy), which is converted to a photon number spectrum. This approach leads to the expression for predicted flux density, $f_{\nu_i}^{\mathrm{pred}}$, for each broadband filter, i

$$f_{\nu_i}^{\mathrm{pred}}(\mu\mathrm{Jy}) = A\frac{\int\lambda^\beta T_i(\lambda)M(\lambda)\lambda d\lambda}{\int f_\lambda^{\mathrm{ref}}(\lambda)T_i(\lambda)\lambda d\lambda}. \quad (8)$$

We compute a χ^2 for each fit, and we optimize the normalization parameter, A, by selecting the value for which $\partial\chi^2/\partial A = 0$. Finally, the complete, normalized predicted flux in μJy is computed from Equation (8). The above fit procedure is repeated for each trial β value, and the fit with the smallest χ^2 is chosen to represent the data.

The resulting power-law index, β, is then used to compute the UV extinction from the empirical relation of Meurer et al. (1999):

$$A_{1600} = 4.43 + 1.99\beta, \quad (9)$$

which is found to have 0.55 mag dispersion about their fit in A_{1600} and a standard error in the fit zero point of 0.08 mag; see Equation (11) and Figure 1 from Meurer et al. (1999). The UV extinction is then used to correct the measured UV flux according to

$$F_{\mathrm{UV}}^{\mathrm{Corr}} = 10^{0.4A_{1600}}F_{\mathrm{UV}}^{\mathrm{Uncorr}}. \quad (10)$$

Finally, the corrected UV flux is used to estimate the SFR using Equation (7). The above procedure is executed for each s*BzK* galaxy individually as well as for the unweighted average spectrum of all s*BzK*s within a redshift bin, whereby the bin median redshift is used to compute the luminosity distance.

Uncertainties to the corrected UV luminosity arise from observed flux uncertainty, error in the dust correction factor, and photometric redshift error (for individual galaxies, we adopt the value of $\delta z/(1+z) = 0.009$; for the average spectra, this contribution is negligible, as discussed in Section 3.1 and via simulations in Section 3.5). These uncertainties are combined using standard error analysis. We do not include the systematic uncertainty associated with the luminosity–SFR calibration (discussed above, about a factor of two); rather we consider this uncertainty with similar systematics from other waveband estimators separately in Section 5. The results of these computations are shown in Table 5 and discussed in Section 5.

3.3. Radio Luminosity and SFR Estimation

Radio. Radio data at 610 MHz were obtained from the Giant Metrewave Radio Telescope (GMRT) survey of the ECDF-S, which reaches a typical depth of 40 μJy beam^{-1} (Ivison et al. 2010a). 1.4 GHz data were obtained from the Very Large Array (VLA) survey, which covers the ECDF-S to a typical depth of 8 μJy beam^{-1} and includes 464 cataloged sources (Miller et al. 2008).

Flux estimates are found from weighted average image stacking (excluding individual detections, which are included after stacking) as well as median image stacking (of all sources) of the VLA and GMRT data. Median stacking is commonly used to reduce the influence of radio-loud AGNs. We adopt the weighted average method to be consistent with the analysis in other wavebands, and we adopt median stacking for comparison. Making images in the radio regime, where the spatial resolution is relatively high, allows us to conserve flux density that would otherwise be lost due to smearing by astrometric uncertainties and finite bandwidth (chromatic aberration) at the cost of larger flux density uncertainties (Ivison et al. 2007). Radio fluxes, luminosities, and corresponding SFRs are illustrated in Table 6.

Our data include flux measurements, S_ν, at 1.4 GHz and 610 MHz for each of the redshift-binned SEDs. The radio spectral index, $S_\nu \propto \nu^\alpha$ (typical $\alpha \sim -0.8$ for galaxies; e.g., Condon 1992), is estimated for each of our three redshift bins to be -0.74 ± 0.2, -1.20 ± 0.2, 0.06 ± 0.4, respectively. In the higher redshift bins, these computed indices deviate significantly from the $\alpha = -0.8$ for synchrotron emission (e.g., anomalously high 610 MHz flux estimate in the $1.5 < z \leqslant 2.0$ bin). Similarly high fluxes were also reported for galaxies in the range $0 < z < 2$ in Bourne et al. (2011) and interpreted as resulting from AGN contamination at high redshift. Therefore in keeping with other reported literature, we adopt the $\alpha = -0.8$ value in computing luminosities and SFRs.

In estimating radio luminosities, we use the median redshift, z, and the corresponding luminosity distance, D_L, in Mpc to compute the aggregate rest-frame 1.4 GHz luminosity, $L_{\nu,1.4\,\mathrm{GHz}}$ in units of W Hz^{-1}, from the observed frame 1.4 GHz flux, S_ν, in units of μJy according to

$$L_{\nu,1.4\,\mathrm{GHz}} = 9.523\times10^{12}\frac{4\pi D_L^2}{(1+z)^{1+\alpha}}S_{\nu,1.4\,\mathrm{GHz}}. \quad (11)$$

Table 5
Redshift-binned s*BzK* UV Luminosity and SFR Estimates

	Average of Individual Spectra					Average Spectrum
Redshift	$\beta_{\rm fit}$	log(IRX)	A_{1600}	$\rm SFR_{UV}^{Uncorr}$	$\rm SFR_{UV}^{Corr}$	$\rm SFR_{UV}^{Corr}$
(1)	(2)	(3)	(4)	(5)	(6)	(7)
$1.2 < z \leqslant 1.5$	−1.50	1.12	1.44	4 ± 0.1	12 ± 1	10 ± 3
$1.5 < z \leqslant 2.0$	−0.80	2.15	2.84	6 ± 0.3	64 ± 4	36 ± 12
$2.0 < z \leqslant 3.2$	−0.59	2.21	3.26	11 ± 0.8	285 ± 30	65 ± 28

Notes. Column 1 indicates sample redshift range. Columns 2–6 correspond to unweighted averages of results from fitting individual galaxies in each redshift bin. Column 2 indicates the best-fit slope, β, to the f_λ spectrum where $f_\lambda \propto \lambda^\beta$. Column 3 indicates the IR–UV ratio, $\log(S_{\rm IR}/S_{1600})$. Column 4 indicates the attenuation in magnitudes at 1600 Å derived from the best-fit spectral index, β. Columns 5 and 6 refer to SFRs in units of $M_\odot$ yr^{-1}. Column 7 indicates the SFR from IRX-β correction applied to the corresponding (unweighted) redshift-bin-averaged spectrum.

Table 6
Redshift-binned s*BzK* Radio Flux, Luminosity, and SFR Estimates

Redshift Range	$S_{1.4}$ (μJy)	$S_{0.610}$ (μJy)	$L_{1.4} \times 10^{22}$ (W Hz^{-1})	$\rm SFR_{1.4}^{Condon}$ ($M_\odot$ yr^{-1})	$\rm SFR_{1.4}^{Bell}$ ($M_\odot$ yr^{-1})
(1)	(2)	(3)	(4)	(5)	(6)
$1.2 < z \leqslant 1.5$	14.6 (12.1) ± 0.8	26.6 (14.8) ± 5.2	13.9 (11.5) ± 0.8	166 (138) ± 11	76 (64) ± 5
$1.5 < z \leqslant 2.0$	11.7 (8.9) ± 0.7	32.2 (33.2) ± 4.3	19.4 (14.7) ± 1.1	232 (176) ± 16	107 (81) ± 7
$2.0 < z \leqslant 3.3$	15.4 (8.4) ± 0.8	14.6 (17.2) ± 5.3	46.6 (25.3) ± 2.5	560 (303) ± 36	257 (139) ± 17

Notes. Column 1 indicates the sample bin redshift range. Columns 2 and 3 include individual detections and weighted average stacked flux at 1.4 GHz and 610 MHz, respectively. In Columns 2–6, results of median stack of all sources are indicated in parentheses. Column 4 indicates the derived rest frame 1.4 GHz luminosity. Column 5 indicates the computed SFR according to Condon (1992). Column 6 indicates the computed SFR according to Bell (2003).

To estimate SFR from $L_{\nu,1.4\,\rm GHz}$, we use the model of Condon (1992) as implemented in Haarsma et al. (2000) and Dunne et al. (2009). Following the implementation in Haarsma et al. (2000), SFR in units of $M_\odot$ yr^{-1} is a function of frequency in units of GHz, $L_{\nu,1.4\,\rm GHz}$ in units of W Hz^{-1}, scaled by a factor Q and is given by

$$\rm SFR_{1.4\,GHz}^{Condon} = Q \frac{L_\nu^{1.4\,\rm GHz}}{5.3 \times 10^{21} \nu^\alpha + 5.5 \times 10^{20} \nu^{-0.1}}. \quad (12)$$

We use the value $Q = 5.5$ to scale the SFR ($M > 5\,M_\odot$) calculated in Condon (1992) to the SFR (0.1–100 $M_\odot$) used here; this scaling factor depends on the assumed (Salpeter) IMF used here and by Haarsma et al. (2000).

For comparison, we also estimate SFR from 1.4 GHz flux using the calibration of Bell (2003). This calibration is based on the IR–radio correlation; it assumes that nonthermal radio emission directly tracks the SFR and is chosen so that the radio SFR matches the IR SFR for $L \geqslant L^*$ galaxies. The SFR calibration,

$$\rm SFR_{1.4\,GHz}^{Bell}(\mathit{M}_\odot\,yr^{-1}) = 5.52 \times 10^{-22} L_{1.4\,GHz}, \quad (13)$$

is adopted here. A similar calibration is found in Yun et al. (2001). $\rm SFR_{1.4\,GHz}^{Condon}$ exceeds $\rm SFR_{1.4\,GHz}^{Bell}$ by a factor of two; the calibration of Condon (1992) explicitly models the thermal and nonthermal emission mechanisms, whereas the calibration of Bell (2003) relies upon the IR–radio correlation. Thus, we expect agreement between $\rm SFR_{1.4\,GHz}^{Bell}$ and IR-based SFR estimates, if the IR–radio correlation continues to hold at high redshift, as has indeed been suggested in the literature (Sargent et al. 2010; Ivison et al. 2010b).

Uncertainties to the radio luminosities are computed by incorporating uncertainties from redshift and flux measurement; these uncertainties are propagated into the SFR uncertainties. When only flux measurement uncertainties are included in the error budget, uncertainties in $\rm SFR_{1.4\,GHz}^{Condon}$ agree to within 30% of published values (Dunne et al. 2009). In the calibration of Bell (2003), scatter in the IR–radio correlation contributes a factor of 1.8 (dispersion of 0.26 dex for individual galaxies) to the uncertainty and dominates the total error budget; this additional systematic uncertainty arising from the $L_{\rm IR}$–SFR calibration is discussed in Section 5

3.4. X-Ray SFR Estimation

X-ray exposure in the ECDF-S consists of 4 Ms in the central $\approx 16' \times 16'$ CDF-S, reaching approximate sensitivities of 1×10^{-17} and 7×10^{-17} erg cm^{-2} s^{-1} in the 0.5–2.0 and 2.0–8 keV bands, respectively, and giving this field the deepest X-ray coverage to date (Xue et al. 2011). These data are augmented with four flanking 250 ks exposures that complete the $\approx 30' \times 30'$ ECDF-S field and reach sensitivity limits of 1.7×10^{-16} and 3.9×10^{-16} erg cm^{-2} s^{-1} in the 0.5–2.0 and 2.0–8.0 keV bands, respectively (Lehmer et al. 2005; Virani et al. 2006).

X-ray stacking analysis was performed in the 4 Ms CDF-S; due to the ratio of exposure times in the CDF-S versus ECDF-S, the deeper CDF-S data will dominate any stacking signal. The X-ray stacking algorithm is discussed in Treister et al. (2011); a position-dependent aperture correction was used to account for the varying *Chandra* PSF with off-axis angle, and to minimize this correction, only sources within 10′ of the aim point were stacked. Sources that have an X-ray detection closer than 15″ to the stacking position are removed to provide a better estimation of the background. This procedure leaves 19, 29, and 19 source positions in redshift bins from $1.2 < z \leqslant 1.5$, $1.5 < z \leqslant 2.0$, and $2.0 < z \leqslant 3.2$, respectively, that are stacked in *Chandra* soft band and hard band data. Stacked fluxes are combined with

Table 7
Redshift-binned s*BzK* X-Ray Flux, Luminosity, and SFR Estimates

Redshift Range (1)	Flux (0.5–2 keV) (2)	Flux (2–8 keV) (3)	Luminosity (Rest 2–10 keV) (4)	$SFR^{Ranalli}_{2-10\,keV}$ ($M_\odot$ yr^{-1}) (5)	$SFR^{Persic}_{2-10\,keV}$ ($M_\odot$ yr^{-1}) (6)	$SFR^{Lehmer}_{2-10\,keV}$ ($M_\odot$ yr^{-1}) (7)
$1.2 < z \leqslant 1.5$	3.2 ± 1.0	31 ± 21	7 ± 7	15 ± 22	73 ± 67	62 ± 46
$1.5 < z \leqslant 2.0$	7.4 ± 1.2	44 ± 16	29 ± 10	58 ± 75	292 ± 116	291 ± 123
$2.0 < z \leqslant 3.2$	9.5 ± 1.2	27 ± 6	50 ± 14	100 ± 126	499 ± 170	507 ± 203

Notes. Column 1: the sample bin redshift range; Column 2: observed flux density in *Chandra* soft band (0.5–2 keV), in units of 10^{-18} erg s^{-1} cm^{-2}; Column 3: observed flux density in *Chandra* hard band (2–8 keV), in units of 10^{-18} erg s^{-1} cm^{-2}; Column 4: the luminosity in rest frame (2–10 keV), computed from observed, soft band flux, assuming a spectrum with photon index, $\Gamma = 1.2$ and $E_c = 20$ keV, at the median redshift. Units are 10^{40} erg s^{-1}; Column 5: SFR from the method of Ranalli et al. (2003); Column 6: SFR from the method of Persic et al. (2004); Column 7: SFR from the method of Lehmer et al. (2010). All SFRs in units of $M_\odot$ yr^{-1} assuming Salpeter IMF (0.1–100 $M_\odot$).

one individually detected source each in the $1.2 < z \leqslant 1.5$ and $1.5 < z \leqslant 2.0$ bins, according to the procedure in the Appendix. Including these individual detections increased the soft band stacking flux estimate by 33% in the $1.2 < z \leqslant 1.5$ bin and had negligible effect on the $1.5 < z \leqslant 2.0$ bin.

Counts-to-flux and flux-to-luminosity conversions are done assuming a spectrum with photon index $\Gamma = 1.2$ and cutoff energy, $E_c = 20$ keV. The rest-frame 2–10 keV luminosities are used to estimate SFR. As shown by Persic & Rephaeli (2002), the X-ray spectrum of SF galaxies that do not have an AGN is dominated by HMXBs, which are best described by $\Gamma = 1.2$ and a cutoff energy of 20 keV. Many SF galaxies also present a thermal component, which is typically softer in X-rays with $kT \sim 0.7$ keV (Fabbiano 1989). The spectrum of the resulting combination is something softer than a pure $\Gamma = 1.2$, but not quite $\Gamma = 2$. In studying LBGs, Nandra et al. (2002) assumed an intrinsic spectrum of $\Gamma = 2.0$, more typical of local Seyfert galaxies and soft X-ray selected quasars. To estimate the effect of different assumptions of photon spectrum index, we also computed counts to flux and luminosity conversions using $\Gamma = 1.9$. The differences of conversions from counts to flux are ∼11%. Similarly, the differences in conversion from observed frame soft band to rest-frame hard band are ∼16% between these two assumptions of spectral index. Thus, in the soft band the uncertainties due to an assumed spectral shape are ∼20%. X-ray fluxes, luminosities, and SFRs are tabulated in Table 7 and discussed in Section 4.4.

The X-ray–SFR calibration of Ranalli et al. (2003) is widely used and is based upon the X-ray–IR-luminosity correlation observed in galaxies with $L_{2-10\,keV} \lesssim 10^{41}$ erg s^{-1}. The SFR in units of $M_\odot$ yr^{-1} is related to the 2–10 keV luminosity, $L_{2-10\,keV}$ in units of erg s^{-1}, according to

$$SFR^{Ranalli}_{2-10\,keV} = 2.0 \times 10^{-40} L_{2-10\,keV}. \quad (14)$$

This calibration implicitly assumes the L_{IR}–SFR calibration of Kennicutt (1998a) and a Salpeter IMF (0.1–100 $M_\odot$) consistent with other calibrations mentioned in this paper.[15] However, the Ranalli et al. (2003) sample includes few SF galaxies in the ULIRG regime, where the L_X–SFR correlation is observed to drop (B. D. Lehmer 2010, private communication).

The uncertainty to $SFR^{Ranalli}_{2-10\,keV}$ is computed by adding in quadrature uncertainties in X-ray luminosity and the 0.09 dex error of the slope in the X-ray–IR-luminosity correlation (see Ranalli et al. 2003, Equation (10)). Luminosity uncertainties are computed by propagating the flux estimate errors; redshift errors of the average spectrum can be neglected, as discussed in Section 3.1 and shown in simulations discussed in Section 3.5.

Subsequent studies have related instantaneous SFR specifically to luminosity from short-lived HMXBs (e.g., Grimm et al. 2003; Colbert et al. 2004; Persic et al. 2004), while slowly evolving, LMXBs are linked to stellar mass, i.e., integrated SFR (Colbert et al. 2004). The X-ray SFR calibration of Persic et al. (2004) is based upon the luminosity of HMXBs, and it relates SFR in units of $M_\odot$ yr^{-1} to the 2–10 keV HMXB luminosity, $L^{HMXB}_{2-10\,keV}$ in units of erg s^{-1}, according to

$$SFR^{Persic}_{2-10\,keV} = 10^{-39} L^{HMXB}_{2-10\,keV}. \quad (15)$$

The fraction, f, of HMXB X-ray luminosity to the total X-ray luminosity has been estimated as $f \sim 0.2$ (with substantial scatter due to low statistics) for nearby SF galaxies (Persic et al. 2004). For high-redshift ($z > 1$) galaxies, in the absence of definitive estimates from X-ray spectroscopy, the value $f = 1$ has been used on the assumption that LMXBs (or other sources of emission) contribute a negligible fraction to the total X-ray luminosity at $z \sim 2$ (Persic et al. 2004; Persic & Rephaeli 2007).

Assuming $f = 0.2$ for nearby SF galaxies leads to $L^{HMXB}_{2-10\,keV} = 0.2\, L^{Total}_{2-10\,keV}$, which brings the calibration of Persic et al. (2004) into equivalence with the calibration of Ranalli et al. (2003). Our data for high-redshift galaxies do not directly constrain the HMXB luminosity fraction; with the assumption $f = 1$, $L^{HMXB}_{2-10\,keV} = L^{Total}_{2-10\,keV}$, and the SFRs estimated from Persic et al. (2004) exceed those of Ranalli et al. (2003) by a factor of five. In computing SFR, we adopt $f = 1$ for the X-ray calibration of Persic et al. (2004) for our sample of s*BzK*s, and we regard the resulting SFRs as upper limits.

The relative contribution of LMXBs to the total X-ray luminosity is believed to decline above $z \sim 1$ (Ghosh & White 2001) and to be subdominant in high SFR (e.g., $>100\,M_\odot$ yr^{-1}) galaxies. A bilinear relation between X-ray luminosity and both SFR and stellar mass, $M_\star$, has been proposed (e.g., Colbert et al. 2004). The X-ray SFR calibration of Lehmer et al. (2010) is derived from such a relationship:

$$L^{Lehmer}_{2-10\,keV} = \alpha M_\star + \beta SFR. \quad (16)$$

In analysis of LIRGs/ULIRGs extending to $L_{2-10\,keV} \sim 10^{41.5}$ erg s^{-1}, Lehmer et al. (2010) report $\alpha = (9.05 \pm 0.37) \times 10^{28}$ erg s^{-1} $M_\odot^{-1}$ and $\beta = (1.62 \pm 0.22) \times 10^{39}$ erg s^{-1} $(M_\odot$ yr$^{-1})^{-1}$. In the absence of the $M_\star$ term in Equation (16), and with the assumption $f = 1$, as discussed above, this calibration becomes consistent to within errors of the calibration of

[15] Note that the radio SFR calibration cited in Ranalli et al. (2003) refers to $M > 5\,M_\odot$ mass range. For a Salpeter IMF, the resulting X-ray–radio derived SFRs differ by a factor of 5.5 from the 0.1–100 $M_\odot$ range used here.

Persic et al. (2004), after accounting for the differences in IMF assumed by these authors.

In order to compute $SFR^{Lehmer}_{2-10\,keV}$, we estimate stellar masses for our redshift-binned s*BzK* samples. We use the empirical correlation between the observed frame *K*-band magnitude and the stellar mass for s*BzK*s at $z > 1.4$, determined from SED fits, that is presented in Daddi et al. (2004):

$$\log(M_\star/10^{11}M_\odot) = -0.4(K^{tot} - K^{11}), \quad (17)$$

where $K^{11} = 21.4$ is the *K*-band magnitude corresponding on average to a stellar mass of $10^{11}\,M_\odot$. Daddi et al. (2004) report uncertainties of ∼40% with this relation.

Uncertainties in $SFR^{Lehmer}_{2-10\,keV}$ are calculated by propagating the uncertainties in the luminosity and stellar mass, along with the reported uncertainties in the parameters α and β indicated above. This calibration is based implicitly on the L_{IR}–SFR calibration of Bell et al. (2005), which yields lower SFRs by ≈13% compared with the corresponding calibration of Kennicutt (1998b); however, we neglect this small calibration difference and discuss systematic uncertainties in comparison with other SFR indicators in Section 5.

3.5. Simulations

We investigate the effects of redshift bin averaging, photometric redshift errors, and dispersion of individual galaxy SEDs on our stacked L_{IR} estimates with simulations. Averaging the photometric flux density from galaxies at slightly different redshifts within a redshift bin introduces redshift smearing. In order to study this effect, we simulate a set of identical CE01 template spectral models. These spectra are shifted to the identical redshifts of galaxies in our $1.5 < z \leqslant 2.0$ redshift bin, and then averaged together, analogous to the actual stacking procedure. The redshift-bin-averaged spectrum is nearly identical to the template spectrum except for moderate smearing of the emission peaks that contributed a negligible amount to the integral; consequently, the quantity of interest, the integrated IR luminosity, is robust against redshift smearing over our bin widths.

Of greater concern is the effect on L_{IR} due to photometric redshift errors and dispersion due to individual galaxy SEDs. To quantify the contribution of these errors to the estimated L_{IR} for each redshift bin, we simulate sets of galaxies with SEDs chosen at random from CE01 templates and distributed in redshift to simulate the observed source distribution. The photometric redshift error distribution is determined from comparison of spectroscopic and photometric redshifts for the subset of sources with both estimates available and is shown in Figure 3. This distribution is well fit by a Gaussian with mean = −0.02 (i.e., bias) and $\sigma = 0.09$ (i.e., scatter). The bias is first removed from the simulated object redshifts, and then artificial redshift errors drawn from this biased, Gaussian distribution are added in each repeated trial of the simulation. The resulting spectra are averaged, and this averaged spectrum is integrated to determine L_{IR}. An example of these spectra from the $1.5 < z \leqslant 2.0$ redshift bin simulation is illustrated in Figure 5. From the figure, it is apparent that the averaged spectrum has a slightly higher flux than the single-object spectrum near the emission peak and therefore will overestimate L_{IR}. For each repeated trial, the fractional error in the L_{IR} estimate is determined by comparing the bin-averaged L_{IR} to the true redshift-bin-averaged luminosity. The frequency distribution of L_{IR} fractional errors is determined directly from 10^4 repeated trials for each redshift bin. The fractional error distributions for redshift bins $1.2 < z \leqslant 1.5$, $1.5 < z \leqslant 2.0$, and $2.0 < z \leqslant 3.2$ are each Gaussian with mean = 12%, 14%, 2% (bias) and σ = 7%, 6%, 6% (scatter), respectively. The fractional error distribution for the $1.5 < z \leqslant 2.0$ bin is illustrated in Figure 5. Our reported values in Table 4 are bias subtracted and have the scatter added in quadrature with other sources of errors.

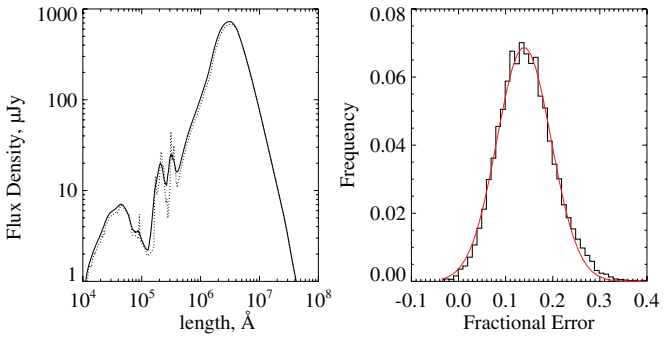

Figure 5. Left panel illustrates simulated, observed frame spectra for s*BzK* galaxies in the range $1.5 < z \leqslant 2.0$. The dotted curve indicates the best-fit CE01 template placed at the median redshift, $z = 1.756$. The solid curve indicates the result of averaging 233 identical CE01 template sources, distributed in redshift according to the observed distribution of s*BzK*s, with photometric redshift errors added according to the distribution shown in Figure 3. The right panel illustrates the frequency distribution of L_{IR} fractional errors due to photometric redshift errors and dispersion from individual galaxy SEDs, for s*BzK* galaxies in the range $1.5 < z \leqslant 2.0$. Solid curve (red) indicates a Gaussian fit with mean = 0.14 and $\sigma = 0.06$. Thus, L_{IR} for this redshift bin is overestimated by 14%; photometric redshift and galaxy SED dispersion contribute a scatter of 6%.

(A color version of this figure is available in the online journal.)

Finally, in simulations we address the issue of whether luminosities computed from the average flux SED taken to be at the median redshift of each bin may accurately reflect the true average luminosity of our sample of individual galaxies. To test this method, we distribute a set of galaxies, with CE01 templates chosen at random, distributed in redshift according to the actual source population, compute the L_{IR} of each galaxy individually, and average them to determine true average L_{IR}. Then for each galaxy, we compute observed frame photometric fluxes in each FIR–radio waveband, and subsequently compute the sample average observed flux SED. We compute the L_{IR} of the average flux SED, assumed to be at the median redshift using the methods of Section 3.1. We compare this L_{IR} estimate with the true average L_{IR} and determine the distribution of errors with 10^3 Monte Carlo realizations.

The fractional error distributions for redshift bins $1.2 < z \leqslant 1.5$, $1.5 < z \leqslant 2.0$, and $2.0 < z \leqslant 3.2$ are each Gaussian with mean = 0.02, 0.09, and 0.02, respectively, and $\sigma = 0.03$ in each case. Thus, the average flux spectrum approximation introduces only a small redshift-dependent bias (which may be removed by using an rms effective redshift for each bin) and a scatter of ∼3% to our L_{IR} estimates. These errors are small especially compared with systematics; therefore, our samples of redshift-binned galaxies are well represented by an average flux SED at the median redshift.

4. RESULTS

4.1. IR SFR Estimates

SFR_{IR} values that are obtained from CE01 template fits are illustrated in Figure 4 and tabulated in Table 4. All of our redshift bins contain significant submillimeter detections, which help to constrain the dust emission peaks. We adopt CE01 template fits in the range $\lambda \geqslant 24\,\mu$m for our preferred L_{IR} values. Though

not formally the best χ^2, they are comparable to the best fits and including the 24 μm photometry makes maximum use of the available data. L_{IR} values obtained from Table 4 are consistent with results of Daddi et al. (2005), who select *BzK*s to the same depth in the *K* band as presented here, and use MIPS 24 μm photometry to estimate $L_{IR} \sim 1.7 \times 10^{12}$ erg s^{-1} for *BzK*s in the range $1.4 < z < 2.5$.

4.2. UV SFR Estimates

Table 5 illustrates the unweighted averages of estimates of UV SFRs from analysis of individual s*BzK* galaxies in each redshift bin. Averages excluded galaxies with poor fits to the spectral index, β, identified by large χ^2 ($\chi^2_\nu > 2$) or best-fit β values that were pinned at the extreme of the allowed parameter range. In our three redshift bins $1.2 < z \leqslant 1.5$, $1.5 < z \leqslant 2.0$, and $2.0 < z \leqslant 3.3$, these poor fit criteria excluded 41, 82, and 48 galaxies, respectively, from the averages. Average $\mathrm{SFR}_{\mathrm{UV}}^{\mathrm{Corr}}$ is in the range 12–285 $M_\odot$ yr^{-1}, increasing with redshift. SFR in the highest redshift bin is affected by outliers; the median $\mathrm{SFR}_{\mathrm{UV}}^{\mathrm{Corr}}$ for individual galaxies are 10, 33, and 106 $M_\odot$ yr^{-1} in each redshift bin, respectively. However, in keeping with the literature, we adopt the average of individual fits as our preferred indicator of UV SFRs for our sample.

We also compute the SFRs from a single unweighted average spectrum of galaxies within each redshift bin. These estimates are systematically lower than the averages of individual galaxies in each bin because the best-fit UV continuum slopes to the average spectra indicate a lower dust correction than the average of individual fits. For redshift bins $1.2 < z \leqslant 1.5$, $1.5 < z \leqslant 2.0$, and $2.0 < z \leqslant 3.3$, the fits to average spectra had reduced χ^2 values of 0.3, 1.8, and 3.8 respectively. We interpret these values to mean acceptable fits for the lower two redshift bins.

There are 11 galaxies in the highest redshift bin with SFR > 1000 $M_\odot$ yr^{-1}. Checking the positions of these galaxies against the published LESS catalog (Weiß et al. 2009) indicates that they are not submillimeter sources; separations between these galaxies and their nearest neighbor in the submillimeter catalog are all greater than 50″. Five of these sources are detected in 24 μm waveband, and their inferred luminosities and SFRs (from CE01 fits) are also high ($\mathrm{SFR}_{24\,\mu\mathrm{m}} > 600\ M_\odot$ yr^{-1}); however, as discussed below, $\mathrm{SFR}_{24\,\mu\mathrm{m}}$ is known to be overestimated in this redshift and luminosity range. One of these sources is detected in radio, with $L_{1.4\,\mathrm{GHz}} = 3 \times 10^{24}$ W Hz^{-1} ($\mathrm{SFR}_{1.4\,\mathrm{GHz}}^{\mathrm{Bell}} = 1650\ M_\odot$ yr^{-1}), and therefore may be an example of previously reported optically faint radio galaxies (OFRGs; Chapman et al. 2004; Casey et al. 2009).

IRAC colors are available for 3 of these 11 galaxies, and none of them appear in the AGN selection region of Stern et al. (2005) in IRAC color–color space. None of these sources are individually detected in X rays, although three of them are within the CDF-S (between 5′–10′ from center). AGN contamination cannot be ruled out; however, we would expect obscuration of the AGN in rest-frame UV and optical wavebands to mean that star formation would dominate the emission (as opposed to the case in X-ray wavebands, where obscured AGNs are a dominant confounding factor). These outliers may suggest either different dust physical properties or geometry in these galaxies.

In comparison with other literature works, Daddi et al. (2004) determine SFRs for a $K_{\mathrm{Vega}} < 20$ sample of 24 s*BzK* galaxies in the GOODS-S field at $z > 1.4$ using SED fitting and dust correction using the method of Meurer et al. (1999), and find dust-corrected SFR in the range 100–600 $M_\odot$ yr^{-1}. In a spectroscopically selected sample of *BzK*s, Yoshikawa et al. (2010) find SFRs to vary widely, over three orders of magnitude.

4.3. Radio SFR Estimates

Radio fluxes, luminosities, and associated SFRs are reported in Table 6 and radio SFRs are compared to calibrations in other wavebands in Table 8. It has been reported previously that $\mathrm{SFR}_{1.4\,\mathrm{GHz}}^{\mathrm{Condon}}$ exceeds $\mathrm{SFR}_{1.4\,\mathrm{GHz}}^{\mathrm{Bell}}$ by approximately a factor of two (Bell 2003). Discrepancies between the radio SFR calibrations of Bell (2003) and Condon (1992) are not entirely surprising given the different assumptions of each calibration.

Daddi et al. (2005) report radio stacking (weighted average stacking + individual detections) of their $K_{\mathrm{Vega}} < 20$ sample to obtain a luminosity of 3.6×10^{23} W Hz^{-1}, corresponding to SFR $\sim 210\ M_\odot$ yr^{-1}, using the radio calibration of Yun et al. (2001), which is similar to our calibration of Bell (2003). Our estimates from Table 6 are consistent with these results.

In stacking a $K_{\mathrm{AB}} \leqslant 23$ sample of *BzK*s, Dunne et al. (2009) reported a median s*BzK* luminosity of 1.28×10^{23} W Hz^{-1} corresponding to SFR $= 154 \pm 7\ M_\odot$ yr^{-1}, which is similar to our $1.2 < z \leqslant 1.5$ bin result of $138 \pm 11\ M_\odot$ yr^{-1}, although a formal comparison is not possible because of the 1.2 mag shallower depth of this present sample. Likewise, the values presented here are similar to the results from the COSMOS survey ($K_s < 23$ selected sample; SFR in the range 30–100 $M_\odot$ yr^{-1}; Pannella et al. 2009), where the radio–SFR calibration of Yun et al. (2001) is used.

4.4. X-Ray SFR Estimates

Our *Chandra* soft band stacked X-ray fluxes are in the range (3.2–9.5) $\times 10^{-18}$ erg s^{-1} cm^{-2}, see Table 7. Using the observed frame, soft band fluxes, and our assumed $\Gamma = 1.2$ spectrum to convert flux to luminosity leads to rest-frame 2–10 keV luminosities in the range (7–50) $\times 10^{40}$ erg s^{-1}, indicated in Table 7.

In comparison with other reported values of galaxies detected to the same *K*-band depth as presented here, Daddi et al. (2004) find rest-frame 2–10 keV luminosity of 8.6×10^{41} erg s^{-1} (they use $\Gamma = 2.1$ in their flux to luminosity conversion) in stacking 23 s*BzK*s in the K20 Survey (Cimatti et al. 2002) that includes part of the CDF-S. Daddi et al. (2005) find a rest-frame 2–10 keV luminosity of 3.4×10^{41} erg s^{-1} in stacking X-ray undetected s*BzK*s in 2 Ms *Chandra* data in GOODS-N (they use $\Gamma = 2.0$ in their flux to luminosity conversion). Thus, we conclude that our stacked X-ray luminosities are consistent with other $z \sim 2$ SF galaxies reported in the literature.

Our SFRs estimated from the rest-frame 2–10 keV luminosities and the calibration of Ranalli et al. (2003) are in the range 15–100 $M_\odot$ yr^{-1}, a factor of ≈5 lower than the corresponding calibrations of Lehmer et al. (2010) and Persic et al. (2004). As discussed in Section 3.4, $\mathrm{SFR}_{2-10\,\mathrm{keV}}^{\mathrm{Persic}}$ may be considered to provide upper limits. In the SFR calibration of Lehmer et al. (2010), the stellar mass term contributes <23%, 7%, 3%, and 1.4% to the SFRs in each redshift range of Table 8, respectively. The trend of decreasing contribution from LMXBs to the total X-ray luminosity as redshift increases is broadly consistent with models of the LMXB population and star formation history that predict the LMXB population to decline at $z > 1$ (Ghosh & White 2001).

Table 8
Redshift-binned s*BzK* Star Formation Rate Summary

Redshift (1)	SFR_{IR} (2)	$SFR_{24\,\mu m}$ (3)	SFR_{UV}^{Corr} (4)	$SFR_{1.4\,GHz}^{Condon}$ (5)	$SFR_{1.4\,GHz}^{Bell}$ (6)	$SFR_{2-10\,keV}^{Ranalli}$ (7)	$SFR_{2-10\,keV}^{Persic}$ (8)	$SFR_{2-10\,keV}^{Lehmer}$ (9)	SFR_{IR+UV} (10)
$1.2 < z \leqslant 1.5$	$\mathbf{51 \pm 5}$	$\mathbf{79 \pm 9}$	12 ± 1	138 ± 11	$\mathbf{64 \pm 5}$	15 ± 22	73 ± 67	62 ± 46	$\mathbf{55 \pm 6}$
$1.5 < z \leqslant 2.0$	$\mathbf{68 \pm 7}$	$\mathbf{172 \pm 51}$	$\mathbf{64 \pm 4}$	176 ± 16	$\mathbf{81 \pm 7}$	$\mathbf{58 \pm 75}$	292 ± 116	291 ± 123	$\mathbf{74 \pm 8}$
$2.0 < z \leqslant 3.2$	$\mathbf{143 \pm 12}$	620 ± 85	285 ± 30	303 ± 36	$\mathbf{139 \pm 17}$	100 ± 126	499 ± 170	507 ± 203	$\mathbf{154 \pm 17}$

Notes. Star formation rates for redshift-binned s*BzK*s. Column 1: sample redshift range; Column 2: SFR from integrated IR luminosity using CE01 template fits to MIR–radio photometry ($\lambda \geqslant 24\,\mu$m); Column 3: SFR from CE01 template fit to 24 μm data only; Column 4: SFR from average of individual fits to UV continuum with dust correction; Columns 5 and 6: SFR from median, stacked 1.4 GHz flux using the method of Condon (1992) and Bell (2003), respectively; Columns 7–9: SFR from soft band X-ray data using the method of Ranalli et al. (2003), Persic et al. (2004), and Lehmer et al. (2010), respectively; Column 10: the total SFR from the sum of Column 2 and corresponding uncorrected UV SFRs taken from Table 5. Units are $M_\odot$ yr^{-1} for all columns. Values in boldface fall within 2σ of the best estimate, SFR_{IR+UV}. Errors do not include substantial systematic uncertainty, as discussed in the text.

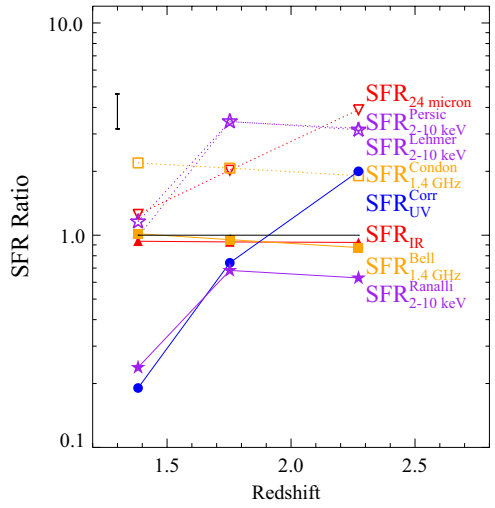

Figure 6. Ratio of SFR computed with various calibrations to the bolometric SFR estimate, SFR_{IR+UV}. Symbols are color coded by waveband: X-ray (purple), UV (blue), IR (red), and radio (orange). Lines connecting points are a guide to the eye. A typical error bar for non-X-ray indicators is illustrated at left. X-ray indicators have larger errors by a factor of ∼2.

(A color version of this figure is available in the online journal.)

5. DISCUSSION

5.1. Comparison of SFR Estimates

SFR estimates from X-ray through radio calibrations are compared in Table 8. The SFR_{IR} values in Table 8 are obtained from L_{IR} estimates from fits of MIR–radio ($\lambda \geqslant 24\,\mu$m) photometry to CE01 templates. To gauge their consistency, we plot the ratio of SFR computed from each calibration to SFR_{IR+UV} in Figure 6. In this figure, SFR_{IR}/SFR_{IR+UV} is most nearly equal to one, reflecting that IR luminosity accounts for >90% of the total SFR in these galaxies.

Comparing $SFR_{24\,\mu m}$ to SFR_{IR+UV} in Table 8 and Figure 6 illustrates the overestimate of SFR at high redshift from this single waveband estimate. The resulting poor fit to the data in the highest redshift bin, $2.0 < z \leqslant 3.2$, illustrated in Figure 4, overestimates L_{IR} by approximately a factor of six. Although 24 μm estimates of L_{IR} can be robust at $z < 1.5$ (e.g., Elbaz et al. 2010), overestimation of L_{IR}, particularly at higher redshift, has been previously reported (e.g., Papovich et al. 2007; Murphy et al. 2009; Muzzin et al. 2010; Nordon et al. 2010; Elbaz et al. 2011). Using *Spitzer* IRS spectroscopy, Murphy et al. (2009) concluded that this luminosity overestimate arises due to unusually large polycyclic aromatic hydrocarbon features in these galaxies, and to a lesser extent, AGN contamination.

Dust-corrected UV SFRs, shown in Table 5, from individual fits to s*BzK* photometry agree with SFR_{IR+UV} in the middle redshift bin, although the highest redshift bin exhibits larger SFR_{UV}^{Corr} and also larger error than lower redshift bins. This large SFR value is strongly affected by a small number of outliers with very high computed SFRs, which may suggest a modified extinction law for at least some galaxies above $z \sim 2$. Also, we find SFR_{UV}^{Corr} to underestimate SFR_{IR+UV} in the lowest redshift bin by a factor of five. SFR_{UV}^{Corr} values were computed using fits to the entire available broadband and medium band photometry (typically 12–14 sampled points in each fit); however, fits that were computed based upon broadband photometry only (typically only three measured points in each fit) produced systematically higher SFRs. The medium band photometry clearly better samples the observed SED, and these results suggest a discrepancy between SFR_{UV}^{Corr} and SFR_{IR+UV} for *BzK*s in this redshift range.

Agreement between dust-corrected UV SFR and SFR_{IR+UV} in *BzK*s to within a factor of ∼ 2 has been reported previously (e.g., Reddy et al. 2006; Daddi et al. 2007b; Nordon et al. 2010). Reddy et al. (2010) find SFR_{UV}^{Corr} to agree with SFR determined from Hα spectroscopy for LBGs at $z \sim 2$. In particular, Reddy et al. (2006) find LBGs and *BzK*s with ages >100 Myr to follow the Meurer et al. (1999) relation while LBGs and *BzK*s with ages <100 Myr have rest UV colors that are redder than expected for a given L_{IR+UV}.

We have tried two methods of estimating radio fluxes: weighted average stacking of non-detections averaged with individual detections and median stacking of all sources. We find results of median stacking to be more consistent with SFR_{IR+UV}, despite the fact that SFR_{IR+UV} estimates were obtained with the method of weighted average stacking. Radio outliers in our sample may be due to residual AGN contamination.

Among radio-based SFR estimates, Figure 6 illustrates agreement between $SFR_{1.4\,GHz}^{Bell}$ and SFR_{IR+UV} to within a factor of two over our redshift range; this agreement is a consequence of the IR–radio correlation for s*BzK*s, which is assumed in the calibration of $SFR_{1.4\,GHz}^{Bell}$. The model of Condon (1992) does estimate star formation from radio luminosity independent of the IR–radio correlation; $SFR_{1.4\,GHz}^{Condon}$ exceeds SFR_{IR+UV} by a factor of two over the observed redshift range, but the ratio of these two calibrations appears relatively insensitive to redshift. The discrepancies between the radio SFR calibrations of Bell (2003) and Condon (1992) are not entirely surprising given the different assumptions of each calibration.

X-ray SFR indicators show wide variation in their ratios to SFR_{IR+UV}. As discussed in Section 4.4, $SFR^{Persic}_{2-10\,keV}$ may be interpreted as an upper limit. $SFR^{Lehmer}_{2-10\,keV}$ yields estimates that are similar to $SFR^{Persic}_{2-10\,keV}$ because of the subdominant contribution of the stellar mass term to the X-ray luminosity in these galaxies. Meanwhile, $SFR^{Ranalli}_{2-10\,keV}$ actually agrees with SFR_{IR+UV} to within a factor of two for $z > 1.5$. $SFR^{Ranalli}_{2-10\,keV}$ has been applied to *BzK*s (e.g., Daddi et al. 2007a; Reddy et al. 2005), BX/BM galaxies (e.g., Reddy & Yun 2004), and LBGs at $z \sim 2$ (e.g., Reddy et al. 2010). In these studies, X-ray SFRs often agree with other waveband estimators, typically to within the same factors as reported here.

However, interpretation of these X-ray SFRs depends upon an uncertain contamination fraction from obscured AGNs. We speculate that AGN contamination may be present in our sample, particularly in the highest redshift bin, in which we find $L_{2-10\,keV} \sim 10^{42}$ erg s^{-1}. AGN contamination even at the level of 10% can require downward adjustment to X-ray SFRs by a factor of 2–5 (Lehmer et al. 2008). Consequently, X-ray SFRs would be overestimated. Lehmer et al. (2008) compute a luminosity-dependent AGN fraction in order to correct X-ray stacking results in $z \sim 3$ galaxies; they find that ≈50%–70% of the stacked 0.5–2 keV counts may arise from obscured AGNs. If a similar AGN fraction exists in our sample, then the X-ray SFRs would need to be adjusted downward by a factor of ∼2.5, bringing $SFR^{Persic}_{2-10\,keV}$ and $SFR^{Lehmer}_{2-10\,keV}$ into better agreement with other waveband indicators, and taking $SFR^{Ranalli}_{2-10\,keV}$ out of agreement with other waveband indicators.

5.2. Sources of Uncertainty

In computing uncertainties in these SFR estimates, we have considered the effects of errors in photometry, spectral shape, and redshift on luminosity estimates. These errors are reported in Table 8 and indicate a wide range in precision of the various waveband indicators. IR estimates are the most precise; X-ray SFR calibrations are the least precise because they rely upon empirical correlations with IR luminosity and thus introduce additional scatter into the SFR estimate. Each of these SFR calibrations assume continuous star formation of at least 10^8 Myr and solar metallicity; therefore, different assumptions about timescales or chemical evolution cannot account for systematic differences between the calibrations.

We have excluded the uncertainty due to luminosity–SFR calibration. We are not able to assess the absolute uncertainties in these SFR calibrations because in many cases they contain implicit dependencies on L_{IR}–SFR calibration. SFR_{IR}, $SFR_{24\,\mu m}$, $SFR^{Bell}_{1.4\,GHz}$, $SFR^{Ranalli}_{2-10\,keV}$, and $SFR^{Persic}_{2-10\,keV}$ depend implicitly upon the L_{IR}–SFR calibration of Kennicutt (1998b), which has a reported systematic uncertainty of about a factor of 2–3. Similarly, $SFR^{Lehmer}_{2-10\,keV}$ depends upon the L_{IR}–SFR calibration of Bell et al. (2005), which also has a reported systematic uncertainty of a factor of two. Similarly, SFR^{Corr}_{UV} depends upon a model-dependent UV-luminosity–SFR calibration for which various published values may differ by a factor of two (Kennicutt 1998a). In the comparisons discussed here, we assume that the various SFR calibrations are consistent with each other and do not evolve with redshift. We compare them against each other, and disagreement can provide evidence of systematic offsets in a given calibration.

For generalizing the results of this sample of *BzK*s to the general population of *BzK*s, errors may be estimated from bootstrap resampling, which would incorporate sample variance, and undoubtedly increase the size of random errors. We do not consider this sample variance here because our primary aim is to compare the SFR calibrations to each other, to assess their consistency, rather than comparing SFRs of *BzK*s as a population to other populations of SF galaxies.

We consider the differing sensitivities to star formation among the various wavebands. We estimate the lowest average SFR detectable in each waveband and redshift bin from the reported image depths by computing the average flux that would yield a 3σ stacked detection given our sample sizes. Converting this flux to a minimum detectable average luminosity at each bin median redshift yields SFR values $<3, \sim 3,$ and $\sim 15\,M_\odot$ yr^{-1} for SFR^{Uncorr}_{UV}, $SFR_{24\,\mu m}$, and SFR_{Radio}, respectively, at all sampled redshifts. SFR^{Corr}_{UV} and SFR_{IR} are even more sensitive than SFR^{Uncorr}_{UV} and $SFR_{24\,\mu m}$; quantitative estimate would require detailed modeling of the SED fitting procedure. The X-ray calibrations are less sensitive, with minimum detectable SFR in the range 30–66 and 150–330 $M_\odot$ yr^{-1} (increasing with redshift) for $SFR^{Ranalli}_{2-10\,keV}$ and $SFR^{Persic}_{2-10\,keV}$, respectively. X-ray SFR estimators have low sensitivity and are subject to bias due to residual AGN contamination and it is not clear which of these effects explains the overestimation of SFR.

6. CONCLUSION

The main results of this paper are summarized in the comparison of SFR indicators given by Table 8 and Figure 6. We consider SFR determined from panchromatic estimation of L_{IR} the most comprehensive approach, where the available data exist, notwithstanding the challenges of accurate fitting of spectral templates. With this method, average SFR of redshift-binned galaxies can be determined with ∼5%–10% random uncertainty (though considerably larger for individual sources); however, the total error is dominated by a factor of ∼2 systematic uncertainty.

This systematic uncertainty, not included in the errors indicated here, of a factor of ∼2 is present in the L_{IR}–SFR and L_{UV}–SFR calibrations that underlie each method of SFR estimation. Each of the calibrations discussed in this paper either implicitly or explicitly assumes a continuous star formation history and solar metallicity; consequently differing assumptions about these parameters should not account for systematic differences.

We find that dust-corrected UV SFR, using the method of Meurer et al. (1999), agrees with SFR_{IR+UV} for galaxies in the range $1.2 < z \leqslant 1.5$, but overestimates SFR_{IR+UV} in the range $2.0 < z \leqslant 3.2$ due to a small population of outliers. Radio SFRs estimated from the calibration of Bell (2003) are in agreement with the total SFRs to within errors. The SFR calibration of Condon (1992) overestimates the total SFR by a factor of two for *BzK* galaxies over this redshift range.

Perhaps surprisingly, the calibration of Ranalli et al. (2003) yields SFR estimates that agree with SFR_{IR+UV} and other indicators in the range $1.5 < z \leqslant 3.2$, while the better suited X-ray calibrations of Persic et al. (2004) and Lehmer et al. (2010) overestimate SFR in the range $1.5 < z < 3.2$. One possible explanation is mild AGN contamination in the upper two bins, which would bring $SFR^{Persic}_{2-10\,keV}$ and $SFR^{Lehmer}_{2-10\,keV}$ into rough agreement with SFR_{IR+UV} and cause $SFR^{Ranalli}_{2-10\,keV}$ to underestimate SFR. X-ray SFR estimates are also notably less sensitive than other waveband indicators.

There is an evident variation in the accuracy and precision of SFR calibrations, and each method has its limitations and

caveats. Radio and X-ray SFR calibrations rely upon empirical correlations of flux in their wavebands to $L_{\rm IR}$ that introduce inevitable scatter, particularly in the X-ray calibrations. 24 μm only and UV SFRs work for most galaxies but have important exceptions and cannot be applied universally.

Our analysis of $K_{\rm AB} < 21.8$ s*BzK*s in the redshift range $1.2 < z \leqslant 3.2$ confirms that they are IR luminous, SF galaxies for which approximately 90% of the total star formation is obscured by dust. By fitting to CE01 templates, we find average IR luminosities for redshift-binned s*BzK* galaxies at median redshifts 1.4, 1.8, and 2.2 to be $(3.0 \pm 0.3) \times 10^{11}\ L_{\odot}$, $(4.0 \pm 0.4) \times 10^{11}\ L_{\odot}$, and $(8.3 \pm 0.7) \times 10^{11}\ L_{\odot}$. We find $\mathrm{SFR_{IR+UV}}$ at these redshifts to be 55 ± 6, 74 ± 8, and $154 \pm 17\ M_{\odot}\ \mathrm{yr}^{-1}$, respectively.

We acknowledge valuable conversations with and comments by Viviana Acquaviva, Eric Bell, Nicholas Bond, Lucia Guaita, Bret Lehmer, Felipe Menanteau, and Axel Weiss, and we thank LESS for providing the 870 μm data, obtained from LABOCA APEX RUN IDs: 078.F-9028(A), 079.F-9500(A), 080.A-3023(A), and 081.F-9500(A). Support for this work was provided by the National Science Foundation under grants AST-0807570 and AST-1055919 and by NASA through an award issued by JPL/Caltech. E.G. thanks U.C. Davis for hospitality during the preparation of this manuscript. Support for the work of E.T. was provided by the National Aeronautics and Space Administration through Chandra Postdoctoral Fellowship Award Number PF8-90055 issued by the Chandra X-ray Observatory Center, which is operated by the Smithsonian Astrophysical Observatory on behalf of the National Aeronautics and Space Administration under contract NAS8-03060.

APPENDIX

ERROR ESTIMATION IN STACKING

A.1. Ordinary Average

Section 3 presents the method used in this paper for estimating the aggregate flux, μ, from N prior positions that include a combination of I individual detections, x_i, and a stacking detection, x_S, from S undetected sources, where $N = I + S$, given by

$$\mu = \frac{1}{N}\left(\sum_{i=1}^{I} x_i + S x_s\right). \tag{A1}$$

The variance σ_μ^2 of this estimate is related to the individual errors σ_i and σ_s as well as their covariances, $\sigma_{i,s}$ from standard error analysis:

$$\sigma_\mu^2 = \sum_{i=1}^{I}\left(\frac{\partial\mu}{\partial x_i}\right)^2\sigma_{x_i}^2 + \left(\frac{\partial\mu}{\partial x_s}\right)^2\sigma_{x_s}^2 + \sum_{i=1}^{I} 2\sigma_{i,s}^2\frac{\partial\mu}{\partial x_i}\frac{\partial\mu}{\partial x_s} + \cdots \tag{A2}$$

We assume that the covariances between individual detections and the stacking detection, $\sigma_{i,s}$, and the covariances between separate individual detections, $\sigma_{i,j}$, are zero:

$$\sigma_\mu^2 = \sum_{i=1}^{I}\left(\frac{\partial\mu}{\partial x_i}\right)^2\sigma_{x_i}^2 + \left(\frac{\partial\mu}{\partial x_s}\right)^2\sigma_{x_s}^2 \tag{A3}$$

$$\sigma_\mu^2 = \frac{1}{N^2}\sum_{i=1}^{I}\sigma_{x_i}^2 + \left(\frac{S}{N}\right)^2\sigma_{x_s}^2 \tag{A4}$$

$$\sigma_\mu = \frac{1}{N}\sqrt{\sum_{i=1}^{I}\sigma_{x_i}^2 + S^2\sigma_{x_s}^2}. \tag{A5}$$

Equations (A1) and (A5) are used to compute the average and error, respectively, of individual and stacking detections reported in this paper.

In the case of all measurement errors being equal, which is a good approximation in the case of LESS data, then $\sigma_i \equiv \sigma$ and $\sigma_s = \sigma/\sqrt{N}$. Using Equation (A5), σ_μ is computed as

$$\sigma_\mu = \frac{1}{N}\sqrt{\sum_{i=1}^{I}\sigma^2 + S^2\frac{\sigma^2}{S}} \tag{A6}$$

$$\sigma_\mu = \frac{1}{I+S}\sqrt{I\sigma^2 + S\sigma^2} \tag{A7}$$

$$\sigma_\mu = \frac{1}{\sqrt{I+S}}\sigma. \tag{A8}$$

A.2. Weighted Average

An alternative approach to combining individual and stacking detections into a single aggregate flux estimate is to use a weighted average of individual and stacking detections. Assume there are $N = I + 1$ flux measurements consisting of I individual detections and a single stacking detection. Each individual flux measurement and the stacked flux measurement are considered as an independent flux measurement for the purpose of computing an average, and these measurements are combined as an inverse variance weighted average:

$$\mu' = \frac{\sum_{i=1}^{N}\frac{x_i}{\sigma_i^2}}{\sum_{i=1}^{N}\frac{1}{\sigma_i^2}} \tag{A9}$$

$$\sigma_{\mu'}^2 = \frac{1}{\sum\frac{1}{\sigma_i^2}}. \tag{A10}$$

Equations (A9) and (A10) are also used to estimate the aggregate flux and error for representative data reported in this paper. In particular, the errors computed according to this method are numerically equal to the errors computed from the ordinary average, Equation (A5), to better than three significant digits.

For clarity, Equation (A10) can be written to include stacking and individual detections separately:

$$\sigma_{\mu'}^2 = \frac{1}{\sum_{i=1}^{I}\frac{1}{\sigma_i^2} + \frac{1}{\sigma_s^2}}. \tag{A11}$$

In the case of all measurement errors being equal, Equation (A11) can be simplified using $\sigma_i \equiv \sigma$ and $\sigma_s = \sigma/\sqrt{N}$, just as in the ordinary average error computation:

$$\sigma_{\mu'}^2 = \frac{1}{\sum_{i=1}^{I}\frac{1}{\sigma^2} + \frac{S}{\sigma^2}} \tag{A12}$$

$$\sigma_{\mu'}^2 = \frac{\sigma^2}{I+S} \tag{A13}$$

$$\sigma_{\mu'} = \frac{\sigma}{\sqrt{I+S}}. \tag{A14}$$

Thus for the case of all measurement errors being equal, the error of the weighted average is identical to the error of the ordinary average.

A.3. Comparison of Ordinary and Weighted Average

In the case of identical errors for the individual measurements, $\sigma_i \equiv \sigma$, then weighted and ordinary averages give the same result for the aggregate flux. In the case of measurement errors being unequal, then the weighted average will in principle have the smaller error; however, the difference will be small, and if the errors are not independent, e.g., if brighter sources have larger errors, then the weighted average introduces a bias to the flux estimate μ'. For instance, if dim sources are always measured with better precision than bright sources, then a weighted average of the population of all sources will always be biased toward dim sources. This circumstance could arise if flux measurement errors are dominated by Poisson counting statistics. However, if the flux measurement errors are uncorrelated with the flux, then there will be no problem with the weighted average.

REFERENCES

Adelberger, K. L., & Steidel, C. C. 2000, ApJ, 544, 218
Bell, E. F. 2003, ApJ, 586, 794
Bell, E. F., Papovich, C., Wolf, C., et al. 2005, ApJ, 625, 23
Biggs, A. D., Ivison, R. J., Ibar, E., et al. 2011, MNRAS, 413, 2314
Blanc, G. A., Lira, P., Barrientos, L. F., et al. 2008, ApJ, 681, 1099
Bourne, N., Dunne, L., Ivison, R. J., et al. 2011, MNRAS, 410, 1155
Brammer, G. B., van Dokkum, P. G., & Coppi, P. 2008, ApJ, 686, 1503
Buat, V., Giovannoli, E., Burgarella, D., et al. 2010, MNRAS, 409, L1
Calzetti, D., Kinney, A. L., & Storchi-Bergmann, T. 1994, ApJ, 429, 582
Cardamone, C. N., van Dokkum, P. G., Urry, C. M., et al. 2010, ApJS, 189, 270
Casey, C. M., Chapman, S. C., Beswick, R. J., et al. 2009, MNRAS, 399, 121
Chapman, S. C., Smail, I., Blain, A. W., & Ivison, R. J. 2004, ApJ, 614, 671
Chary, R., & Elbaz, D. 2001, ApJ, 556, 562
Chary, R.-R., & Pope, A. 2010, arXiv:1003.1731
Cimatti, A., Daddi, E., Mignoli, M., et al. 2002, A&A, 381, L68
Colbert, E. J. M., Heckman, T. M., Ptak, A. F., Strickland, D. K., & Weaver, K. A. 2004, ApJ, 602, 231
Condon, J. J. 1974, ApJ, 188, 279
Condon, J. J. 1992, ARA&A, 30, 575
Daddi, E., Alexander, D. M., Dickinson, M., et al. 2007a, ApJ, 670, 173
Daddi, E., Cimatti, A., Renzini, A., et al. 2004, ApJ, 617, 746
Daddi, E., Dickinson, M., Chary, R., et al. 2005, ApJ, 631, L13
Daddi, E., Dickinson, M., Morrison, G., et al. 2007b, ApJ, 670, 156
Damen, M., Labbe, I., van Dokkum, P., et al. 2011, ApJ, 727, 1
Devlin, M. J., Ade, P. A. R., Aretxaga, I., et al. 2009, Nature, 458, 737
Donley, J. L., Koekemoer, A. M., Brusa, M., et al. 2012, ApJ, 748, 142
Dunne, L., Ivison, R. J., Maddox, S., et al. 2009, MNRAS, 394, 3
Elbaz, D., Dickinson, M., Hwang, H. S., et al. 2011, A&A, 533, A119
Elbaz, D., Hwang, H. S., Magnelli, B., et al. 2010, A&A, 518, L29
Fabbiano, G. 1989, ARA&A, 27, 87
Gawiser, E., van Dokkum, P. G., Herrera, D., et al. 2006, ApJS, 162, 1
Ghosh, P., & White, N. E. 2001, ApJ, 559, L97
Grazian, A., Salimbeni, S., Pentericci, L., et al. 2007, A&A, 465, 393
Greve, T. R., Weiß, A., Walter, F., et al. 2010, ApJ, 719, 483
Grimm, H., Gilfanov, M., & Sunyaev, R. 2003, MNRAS, 339, 793
Haarsma, D. B., Partridge, R. B., Windhorst, R. A., & Richards, E. A. 2000, ApJ, 544, 641
Hogg, D. W. 2001, AJ, 121, 1207
Hopkins, A. M. 2007, in ASP Conf. Ser. 380, Deepest Astronomical Surveys, ed. J. Afonso et al. (San Francisco, CA: ASP), 423
Howell, J. H., Armus, L., Mazzarella, J. M., et al. 2010, ApJ, 715, 572
Huynh, M. T., Pope, A., Frayer, D. T., & Scott, D. 2007, ApJ, 659, 305
Ivison, R. J., Alexander, D. M., Biggs, A. D., et al. 2010a, MNRAS, 402, 245
Ivison, R. J., Chapman, S. C., Faber, S. M., et al. 2007, ApJ, 660, L77
Ivison, R. J., Magnelli, B., Ibar, E., et al. 2010b, A&A, 518, L31
Kennicutt, R. C., Jr. 1998a, ARA&A, 36, 189
Kennicutt, R. C., Jr. 1998b, ApJ, 498, 541
Kroupa, P. 2001, in ASP Conf. Ser. 228, Dynamics of Star Clusters and the Milky Way, ed. S. Deiters et al. (San Francisco, CA: ASP), 187
Kurczynski, P., & Gawiser, E. 2010, AJ, 139, 1592
Lehmer, B. D., Alexander, D. M., Bauer, F. E., et al. 2010, ApJ, 724, 559
Lehmer, B. D., Brandt, W. N., Alexander, D. M., et al. 2005, ApJS, 161, 21
Lehmer, B. D., Brandt, W. N., Alexander, D. M., et al. 2008, ApJ, 681, 1163
Leitherer, C., & Heckman, T. M. 1995, ApJS, 96, 9
Madau, P. 1995, ApJ, 441, 18
Madau, P., Pozzetti, L., & Dickinson, M. 1998, ApJ, 498, 106
Magdis, G. E., Elbaz, D., Daddi, E., et al. 2010, ApJ, 714, 1740
Magnelli, B., Elbaz, D., Chary, R. R., et al. 2009, A&A, 496, 57
Marsden, G., Ade, P. A. R., Bock, J. J., et al. 2009, ApJ, 707, 1729
Meurer, G. R., Heckman, T. M., & Calzetti, D. 1999, ApJ, 521, 64
Miller, N. A., Fomalont, E. B., Kellermann, K. I., et al. 2008, ApJS, 179, 114
Murphy, E. J., Chary, R., Alexander, D. M., et al. 2009, ApJ, 698, 1380
Muzzin, A., van Dokkum, P., Kriek, M., et al. 2010, ApJ, 725, 742
Nandra, K., Mushotzky, R. F., Arnaud, K., et al. 2002, ApJ, 576, 625
Nordon, R., Lutz, D., Genzel, R., et al. 2012, ApJ, 745, 182
Nordon, R., Lutz, D., Shao, L., et al. 2010, A&A, 518, L24
Overzier, R. A., Heckman, T. M., Wang, J., et al. 2011, ApJ, 726, L7
Pannella, M., Carilli, C. L., Daddi, E., et al. 2009, ApJ, 698, L116
Papovich, C., Rudnick, G., Le Floc'h, E., et al. 2007, ApJ, 668, 45
Persic, M., & Rephaeli, Y. 2002, A&A, 382, 843
Persic, M., & Rephaeli, Y. 2007, A&A, 463, 481
Persic, M., Rephaeli, Y., Braito, V., et al. 2004, A&A, 419, 849
Ranalli, P., Comastri, A., & Setti, G. 2003, A&A, 399, 39
Reddy, N. A., Erb, D. K., Pettini, M., Steidel, C. C., & Shapley, A. E. 2010, ApJ, 712, 1070
Reddy, N. A., Erb, D. K., Steidel, C. C., et al. 2005, ApJ, 633, 748
Reddy, N. A., & Steidel, C. C. 2004, ApJ, 603, L13
Reddy, N. A., Steidel, C. C., Fadda, D., et al. 2006, ApJ, 644, 792
Reddy, N. A., & Yun, M. S. 2004, ApJ, 600, 695
Salpeter, E. E. 1955, ApJ, 121, 161
Sargent, M. T., Schinnerer, E., Murphy, E., et al. 2010, ApJ, 714, L190
Stern, D., Eisenhardt, P., Gorjian, V., et al. 2005, ApJ, 631, 163
Takeuchi, T. T., Buat, V., Heinis, S., et al. 2010, A&A, 514, A4
Taylor, E. N., Franx, M., van Dokkum, P. G., et al. 2009, ApJS, 183, 295
Treister, E., Schawinski, K., Volonteri, M., Natarajan, P., & Gawiser, E. 2011, Nature, 474, 356
Truch, M. D. P., Ade, P. A. R., Bock, J. J., et al. 2008, ApJ, 681, 415
Virani, S. N., Treister, E., Urry, C. M., & Gawiser, E. 2006, AJ, 131, 2373
Weiß, A., Kovacs, A., Coppin, K., et al. 2009, ApJ, 707, 1201
Wuyts, S., Förster Schreiber, N. M., Lutz, D., et al. 2011, ApJ, 738, 106
Xue, Y. Q., Luo, B., Brandt, W. N., et al. 2011, ApJS, 195, 10
Yoshikawa, T., Akiyama, M., Kajisawa, M., et al. 2010, ApJ, 718, 112
Yun, M. S., Reddy, N. A., & Condon, J. J. 2001, ApJ, 554, 803